BROADBAND COHERENT PERFECT ABSORPTION

IN ONE-DIMENSIONAL OPTICAL SYSTEMS

by

MASSIMO MAXIMILIAN L. VILLINGER

MSc ETH, Dept. of Electrical Engineering/ETH, 1965-1970
MBA, INSEAD, 1972-1973

A thesis submitted in partial fulfillment of the requirements
for the degree of Master of Science in Optics & Photonics
in the College of Optics & Photonics (CREOL)
at the University of Central Florida
Orlando, Florida

Spring Term

2015

Major Professor: Ayman Abouraddy

ABSTRACT

Absorption plays a critical role in a variety of optical applications – sometimes it is desirable to minimize it as in optical fibers and waveguides, or to enhance it as in solar cells and photodetectors. We describe here a new optical scheme that controllably produces high optical absorption over a broad wavelength range (hundreds of nm) in systems that have low intrinsic absorption over the same range. This effect, 'coherent perfect absorption' or CPA, arises from a subtle interplay between interference and absorption of two beams incident on a weakly absorbing medium.

In the first part of this study, we present an analytical model that captures the relevant physics of CPA in one-dimensional photonic structures. This model elucidates an absorption-mediated interference effect that underlies CPA – an effect that is normally forbidden in Hermitian systems, but is allowed when conservation of energy is violated due to the inclusion of loss. As a concrete example, we consider a Fabry-Pérot resonator containing a lossy dielectric and confirm this model through a computational study of a 1-micron-thick silicon layer in a cavity formed of dispersive mirrors with aperiodic multilayer design. We confirm that one may achieve 100% absorption in this thin silicon layer (whose intrinsic absorption is only ~ 3%) in the near-infrared.

We then design two device models using few-micron-thick aperiodic planar dielectric mirrors and demonstrate (computationally, as well as experimentally) spectrally flat, coherently enhanced absorption at the theoretical limit in a 2-micron-thick film of polycrystalline silicon

embedded in symmetric and asymmetric cavities. This coherent effect is observed over an octave-spanning wavelength range of ~800 – 1600 nm utilizing incoherent light in the near-infrared, exploiting mirrors that have wavelength-dependent reflectivity devised to counterbalance the decline in silicon's intrinsic absorption at long wavelengths. We anticipate that the design principles established here may be extended to other materials, broader spectral ranges, and large surface areas.

Finally, we study the effect of the angle of incidence on CPA in planar structures. The results of this study point to a path for realizing CPA in such systems continuously over large bandwidths.

To the three women who guided my life

Louise Villinger-Vogelenzang, who shares my life

Camilla Villinger, who gave me life

Gerritjen Vogelenzang – van der Kooi, who helped my life

ACKNOWLEDGMENTS

My thanks go to Prof. Abouraddy, for his guidance throughout this project and his support, which made my thesis work an interesting and relevant learning experience.

I also want to join the team in thanking Joshua Perlstein and Seyfollah Teroghi for assistance with ellipsometric measurements, Fred Goldstein at FTG Software for assistance with the FilmStar software, and Karl George, Sr., Karl George, Jr., and Mark Chase at QTF for the fabrication of the planar devices.

TABLE OF CONTENTS

LIST OF FIGURES

1. INTRODUCTION

Optical absorption at a given wavelength is typically viewed as an intrinsic materials property. New schemes exploiting useful consequences of controlling the spatial distribution of optical losses [1–3], or in combination with judiciously placed optical gain [4, 5], are now emerging as part of the burgeoning effort on non-Hermitian photonic structures [6]. To increase absorption in an optical system, a material with heavy loss may be inserted. However, there are critical scenarios where this approach cannot be exploited. Cost or design considerations may allow for only a thin layer of the lossy material to be included, as in thin-film solar cells. Alternatively, in some arrangements the overall absorption does not increase even when more loss is incorporated, as is the case in certain interferometers.

Coherent perfect absorption (CPA) [7] is a new optical scheme that produces high absorption in systems that have low intrinsic losses [8, 9]. By interfering two beams in a lossy material – typically contained in a multipass interferometer such as a Fabry-Perot (FP) resonator –increased absorption is observed with respect to that experienced by each beam separately. The effect appears counter-intuitive: while a *single* beam is *weakly* absorbed [Fig. 1-1(a)], adding a second beam results in *both beams* being *completely* absorbed [Fig. 1-1(b)]. This *linear* phenomenon has been termed 'lasing-in-reverse' and has been investigated in terms of the mathematical behavior of the poles and zeros of the system scattering matrix.

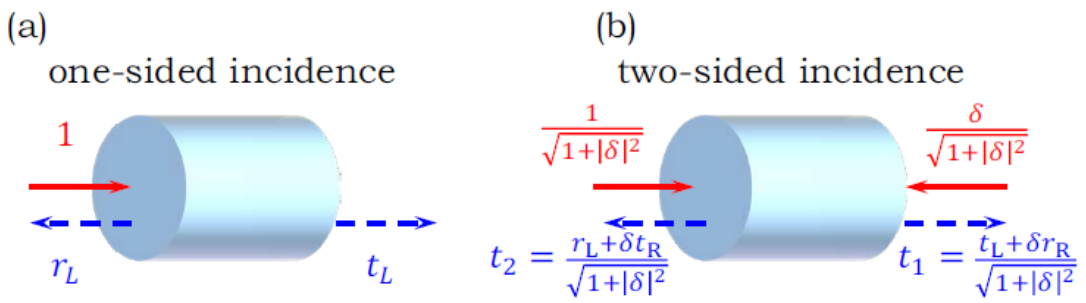

Figure 1-1: (a) Schematic depiction of the one- and (b) two-sided incidence schemes.

In recent years, multiple studies have been published exploring the theoretical properties of time-reversal symmetry of the laser generation process [7,8,9], where resonance in a cavity with a gain medium (negative imaginary refractive index) produces coherent optical radiation of a single frequency. Applying the same equations under time reversal, by replacing the gain medium with an absorbing medium (positive imaginary refractive index), one should expect heightened absorption under resonance conditions [7]. This effect has been theoretically analyzed and experimentally demonstrated in a paper by A. D. Stone et al. [8]. The Si-based experiment in Ref. [8] was carried out tuning a laser over a 3-nm bandwidth in a 100-μm-thick Si film.

It should be pointed out all these CPA studies are based on single-frequency coherent light. Our work introduces radical departures with respect to previous experimental investigations. To date, CPA has been observed only over narrow bandwidths: 3 nm in Ref. [8] and at a single laser wavelength in Refs. [15-17]. Proposals have been made to realize CPA at two distinct wavelengths [18] or over a broad band through modifications of the material's properties (via doping in the case of Si [19]), but experimental observations have not been forthcoming. Our goal here is to address the following challenge: given a specific material, can

one arrange for its effective absorption – without modifying the material itself – to be controllably enhanced beyond its intrinsic absorption over a broad spectrum?

In our work, the design of novel dielectric mirrors extends the CPA bandwidth to a record octave in Si and, crucially, we utilize incoherent – rather than coherent – light, thereby expanding the scope of potential applications. Our strategy for coherently enhancing absorption is amenable to a wide range of materials other than Si and uses only planar technology, readily allowing implementation on large surface areas and flexible substrates.

In this thesis we present an analytical model for achieving CPA with broadband incoherent incident light in one-dimensional (1D) photonic structures using multilayer optics analysis [10–12]. From this perspective, CPA is an absorption-mediated interferometric effect in systems where conservation of energy and reciprocity are violated by including loss. Traditionally, it is thought that losses reduce interferometric visibility. In contrast, absorption in CPA *produces* an interferometric effect that is normally forbidden in lossless structures. Our analytical model, besides its conceptual clarity, provides the basis for optimizing the structure parameters by establishing the general criteria for maximizing CPA. We apply our analysis to a FP resonator consisting of a thin silicon film sandwiched between Bragg mirrors to achieve near-infrared CPA.

Before proceeding to our model, we first present a simple example to illustrate how *adding* a beam to a *linear* passive optical system may *increase* the overall absorption. In Fig. 1-2(a) we depict a balanced Mach-Zehnder interferometer in which a dielectric layer with attenuation factor Υ is placed in one arm.

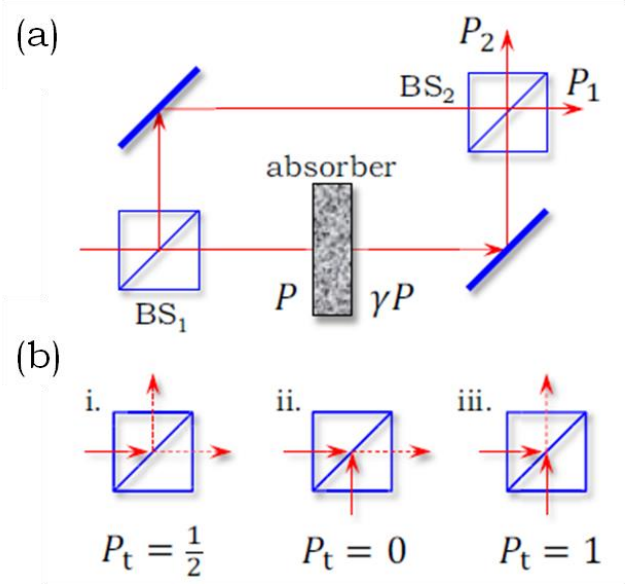

Figure 1-2: (a) Schematic of a balanced Mach-Zehnder interferometer (formed of two symmetric beam splitters BS1 and BS2) with an absorber placed in the lower arm having an absorption factor Y. (b) Three configurations for the beams at the interferometer beam input beam splitter BS1 to control the path the beam is directed to. (i.) The beam is split between the two output ports. (ii.) Two equal-amplitude input beams with an appropriate relative phase are directed together to one port where the lossy element resides. (iii.) The relative phase is changed by π (with respect to ii.) to direct the two beams to the interferometer reference arm.

For symmetric 50/50 beam splitters, the sum of the two interferometer outputs is $P_t = P_1 + P_2 = \frac{1}{2}(1+\gamma)$, and $P_t \to \frac{1}{2}$ for $\gamma \to 0$. If instead the input beam is divided between the two input ports of the interferometer with an appropriate relative phase [Fig. 1-2(b)], then both beams are directed together to one arm, leading either to complete extinction [Pt→0, Fig. 1-2(b)-ii] or zero absorption [Pt=1, Fig. 1-2(b)-iii]. This example highlights that interference *outside* the lossy medium may indeed increase absorption by directing the incident energy solely to the lossy element. We show below that CPA is related to this effect when a low-loss material is placed in a multi-pass configuration.

2. SCATTERING AND TRANSFER MATRIX FORMALISMS

To determine the general criteria for a lossy system to achieve CPA, we consider a generic 1D optical configuration described by a 2×2 scattering matrix **S** [Fig. 2-1]:

$$\mathbf{S} = \begin{pmatrix} s_{11} & s_{12} \\ s_{21} & s_{22} \end{pmatrix} = \begin{pmatrix} t_L & r_R \\ r_L & t_R \end{pmatrix}$$

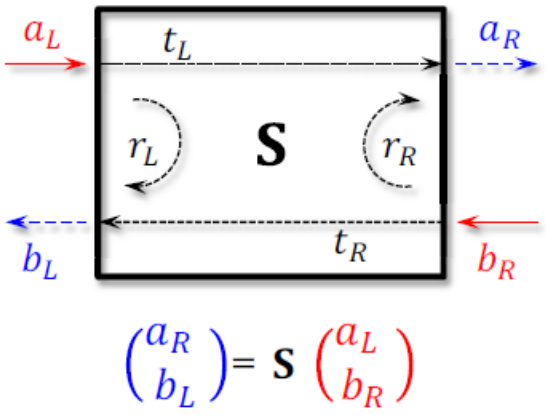

*Figure 2-1: A generic two-port optical system (black box) described by a scattering matrix **S**. The red solid arrows are the inputs (a_L and b_R) and the dashed blue arrows the outputs (b_L and a_R).*

Here t_L, r_L, t_R, r_R are the field transmission and reflection coefficients for left (L) or right (R) incidence. We assume the left and right ambient media are the same for simplicity.

The transfer matrix **T**, on the other hand, relates the field amplitudes in the left and right planes, $\mathbf{T} = \begin{pmatrix} t_{11} & t_{12} \\ t_{21} & t_{22} \end{pmatrix}$. The interrelations between the **S** and **T** representations may be summarized as follows:

$$s_{11} = t_L = \frac{1}{t_{11}}, \qquad s_{12} = r_R = -\frac{t_{12}}{t_{11}}$$

$$s_{21} = r_L = \frac{t_{21}}{t_{11}}, \qquad s_{22} = t_R = \frac{\det \mathbf{T}}{t_{11}}$$

or alternatively:

$$t_{11} = \frac{1}{t_L} = \frac{1}{s_{11}}\ , \qquad t_{12} = -\frac{r_R}{t_L} = -\frac{s_{12}}{s_{11}}$$

$$t_{21} = \frac{r_L}{t_L} = \frac{s_{21}}{s_{11}}\ , \qquad t_{22} = \frac{t_R t_L - r_L r_R}{t_L} = \frac{\det \mathbf{S}}{s_{11}}$$

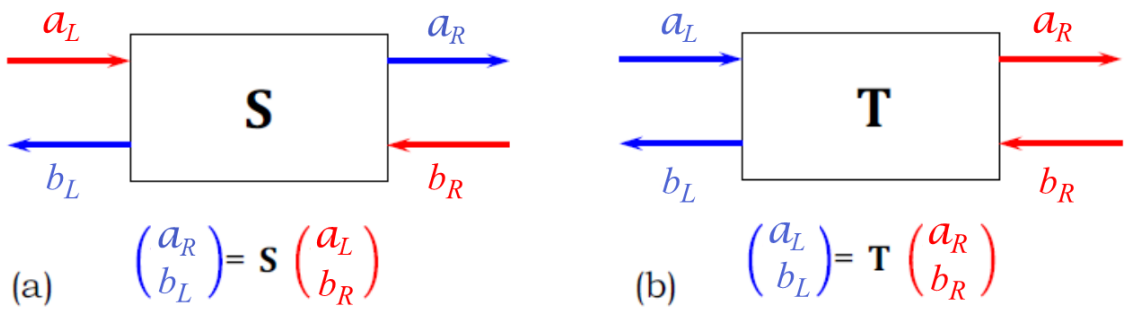

*Figure 2-2: (a) Scattering-matrix **S** and (b) transfer-matrix **T** representations of a two-port system. Red and blue arrows correspond to the input and output amplitudes, respectively, for the linear transformations.*

In general, the scattering matrix **S** is characterized by 8 real parameters, 4 amplitudes and 4 phases for its elements:

$$t_L = |t_L|\, e^{i\beta_L}\ , \quad r_L = |r_L|\, e^{i\alpha_L}$$

$$t_R = |t_R|\, e^{i\beta_R}\ , \quad r_R = |r_R|\, e^{i\alpha_R}$$

As a starting point, we consider a lossless or Hermitian system:

$$a_R = t_L a_L + r_R b_R$$

$$b_L = r_L a_L + t_R b_R$$

Conservation of energy in a such a system implies that:

$$|a_L|^2 + |b_R|^2 = |a_R|^2 + |b_L|^2$$

which results in:

$|t_L|^2 + |r_L|^2 = 1\ ,$ by setting $a_L = 1,\ b_R = 0$

$|t_R|^2 + |r_R|^2 = 1\ ,$ by setting $a_L = 0,\ b_R = 1$

These conditions allow us to eliminate two amplitudes

$t_L = \cos\theta_L e^{i\beta_L}\,, \quad r_L = \sin\theta_L e^{i\alpha_L} \qquad (\theta_L = \beta_L - \alpha_L)$

$t_R = \cos\theta_R e^{i\beta_R}\,, \quad r_R = \sin\theta_R e^{i\alpha_R} \qquad (\theta_R = \beta_R - \alpha_R)$

Furthermore

$$|a_R|^2 + |b_L|^2 = |t_L|^2|a_L|^2 + |r_R|^2|b_R|^2 + |r_L|^2|a_L|^2 + |t_R|^2|b_R|^2 + 2\{(t_L r_R + r_L t_R)a_L b_R\}$$
$$= |a_L|^2(|t_L|^2 + |r_L|^2) + |b_R|^2(|r_R|^2 + |t_R|^2) + 2\Re\{({t_L}^* r_R + {r_L}^* t_R){a_L}^* {b_R}\}\,,$$

which results in:

$\Re\{({t_L}^* r_R + {r_L}^* t_R){a_L}^* {b_R}\} = 0$

for all a_L and b_R. This restriction results in two more conditions:

$\theta_L = -\theta_R = \theta, \quad \beta_L + \beta_R = \alpha_L + \alpha_R$

Which allow us to eliminate one more amplitude and one phase. We now have:

$cos(\theta_L) = cos(\theta) = t\,, \qquad \cos(\theta_R) = \cos(-\theta) = t$

$sin(\theta_L) = sin(\theta) = r\,, \qquad \sin(\theta_R) = \sin(-\theta) = -r$

With $r^2 + t^2 = 1$

$s_{11} = t_L = t\,e^{i\beta_L}\,, \quad s_{12} = r_R = -r\,e^{i(\beta_L+\beta_R-\alpha_L)}$

$s_{21} = r_L = r\,e^{i\alpha_L}\,, \quad s_{22} = t_R = t\,e^{i\beta_R}$

The scattering and transfer matrices can then be written as follows:

$$\mathbf{S} = \begin{pmatrix} t\,e^{i\beta_L} & -r\,e^{i(\beta_L+\beta_R-\alpha_L)} \\ r\,e^{i\alpha_L} & t\,e^{i\beta_R} \end{pmatrix} \quad \text{and} \quad \mathbf{T} = \frac{e^{-i\beta_L}}{t}\begin{pmatrix} 1 & r\,e^{i(\beta_L+\beta_R-\alpha_L)} \\ r\,e^{i\alpha_L} & e^{i(\beta_L+\beta_R)} \end{pmatrix}$$

Note that:

$|t_L| = |t_R| = t \quad \text{and} \quad |r_L| = |r_R| = r \quad \text{and} \quad \det\mathbf{S} = e^{i(\beta_R+\beta_L)}$

$|t_{11}| = |t_{22}| \quad \text{and} \quad |t_{12}| = |t_{21}| \quad \text{and} \quad \det\mathbf{T} = 1$

If there is a relative phase $\emptyset$ between the left and right incident fields, the above conservation of energy condition $\Re\{(t_L{}^* r_R + r_L{}^* t_R) a_L{}^* b_R\} = 0$ can be written as:

$$\Re\{(t_L{}^* r_R + r_L{}^* t_R) e^{i\emptyset}\} = 0 \qquad (2\text{-}1a)$$

with $T_L + R_L = 1 \quad , \quad T_R + R_R = 1$ (2-1b)

where $T_L = |t_L|^2 \, , \quad R_L = |r_L|^2 \, , \quad T_R = |t_R|^2 \, , \quad R_R = |r_R|^2$

A second physical principle, that of **reciprocity**, adds more restrictions.

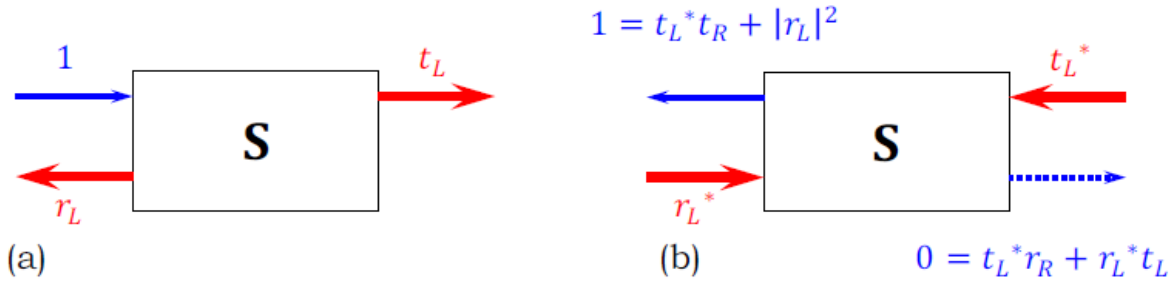

Figure 2-3: (a) Unity input from the left results in outgoing transmitted and reflected waves. (b) Reversing the direction of time such that the outgoing waves become incoming waves (and their amplitudes are thus conjugated). The outgoing waves now must be the incoming waves in (a); that is unity on the left and zero on the right.

As shown in Fig. 2-3, reciprocity implies that reversing the arrow of time should reverse the directions of all the waves without changing the amplitudes. This principle imposes the following two conditions,

$$0 = \mathrm{t_L}{}^* \mathrm{r_R} + r_L{}^* t_L \, , \qquad 1 = \mathrm{t_L}{}^* \mathrm{t_R} + |r_L|^2$$

Consequently,

$$\beta_L = \beta_R = \beta \;\; \rightarrow \;\; 2\beta = \alpha_L + \alpha_R + \pi$$

The form of **S** and **T** under the combined conditions of conservation of energy and reciprocity is,

$$\boldsymbol{S} = \begin{pmatrix} t\, e^{i\beta} & -r\, e^{i(2\beta-\alpha_L)} \\ r\, e^{i\alpha_L} & t\, e^{i\beta} \end{pmatrix} \quad \textit{and} \quad \boldsymbol{T} = \frac{e^{-i\beta}}{t} \begin{pmatrix} 1 & r\, e^{i(2\beta-\alpha_L)} \\ r\, e^{i\alpha_L} & e^{i2\beta} \end{pmatrix} \qquad (2\text{-}2)$$

Note that $\det\mathbf{S} = e^{i2\beta}$ while $\det\mathbf{T} = 1$. As a result, we have $\mathrm{t_L} = \mathrm{t_R}$, $|r_L| = |r_R|$, $t_{11} = t_{22}^*$, $t_{12} = t_{21}^*$.

Finally, if the system is **symmetric**, i.e., the left and right may be seamlessly interchanged, then

$$\alpha_L = \alpha_R = \alpha \qquad \beta_L = \beta_R = \beta \qquad \text{and} \qquad \beta = \alpha + \frac{\pi}{2}$$

$\boldsymbol{S} = e^{i\beta}\begin{pmatrix} t & -re^{i(\beta-\alpha_L)} \\ re^{-i(\beta-\alpha_L)} & t \end{pmatrix} = e^{i\beta}\begin{pmatrix} t & ir \\ ir & t \end{pmatrix}$ and $r^2 + t^2 = 1$, where *r* and *t* are real.

That is, in a lossless symmetric system the reflection and transmission coefficients are in quadrature such that $\Re\{(t_L{}^* r_L)\} = 0$. If fields are incident from the left and right with relative amplitude $\delta = |\delta| e^{i\emptyset}$, which we term hereon *two-sided incidence* [Fig. 1-1(b)], then the normalized fields to the right and left are $t_1 = \frac{t_L + \delta r_R}{\sqrt{1+|\delta|^2}}$ and $t_2 = \frac{r_L + \delta t_R}{\sqrt{1+|\delta|^2}}$, respectively, with $T_1 = |t_1|^2$ and $T_2 = |t_2|^2$.

In considering ***lossy*** systems, the conditions in Eq. 2-1 are no longer satisfied. First, since $T_L + R_L \leq 1$ and $T_R + R_R \leq 1$, we define left and right absorbtivities $\mathcal{A}_L = 1 - \{T_L + R_L\}$ and $\mathcal{A}_R = 1 - \{T_R + R_R\}$, respectively (in general, $\mathcal{A}_L \neq \mathcal{A}_R$). That is, $\mathcal{A}_L$ and $\mathcal{A}_R$ are the fractions of light absorbed upon left *or* right incidence, respectively, which we term one-sided absorption. Furthermore, we ***no longer*** have $\Re\{(t_L{}^* r_R + r_L{}^* t_R) e^{i\emptyset}\} = 0$, and in the case of a symmetric system $\Re\{(t_L{}^* r_L)\} \neq 0$.

For *two*-sided incidence on a **lossy** system, due to interference, the total absorbtivity $\mathcal{A}_T = 1 - \{T_1 + T_2\}$ may not be equal to the weighted sum of $\mathcal{A}_L$ and $\mathcal{A}_R$. For a **symmetric** system ($\mathcal{A}_L = \mathcal{A}_R$), the total absorptivity $\mathcal{A}_T$ is derived as follows:

$$\mathcal{A}_L = 1 - |r_L|^2 - |t_L|^2 \qquad \textit{(2-3)}$$

$$\mathcal{A}_T = 1 - |t_1|^2 - |t_2|^2 \qquad \textit{(2-4)}$$

$$= 1 - \left(\frac{t_L + \delta r_R}{\sqrt{1+|\delta|^2}}\right)^2 - \left(\frac{r_L + \delta t_R}{\sqrt{1+|\delta|^2}}\right)^2, \qquad |t_R| = |t_L| \;\; , \;\; |r_R| = |r_L|$$

$$= 1 - |r_L|^2 - |t_L|^2 - \frac{4|\delta|}{1+|\delta|^2}\Re\{(t_L{}^* r_L)\}\cos\emptyset$$

$$\mathcal{A}_T = \mathcal{A}_L - \frac{4|\delta|}{1+|\delta|^2}\Re\{(t_L{}^* r_L)\}\cos\emptyset \qquad (2\text{-}5)$$

This equation indicates that *two*-sided absorption may be larger or smaller than that expected from *one*-sided absorption – according to the relative phase ϕ of the two beams and the phase $\theta = \beta - \alpha$, $(\alpha = \alpha_L)$, of the *interference* term $\Re\{(t_L{}^* r_L)\}$ This term is normally equal to zero in lossless systems, but may become non-zero when loss is introduced. This *absorption-mediated interference* effect, the second term in Eq. 2-5, is what enables CPA. It is important to note that the interference occurs *outside* the system, just as in the Mach-Zehnder example in Fig. 1-2(a). The normally uncoupled or orthogonal fields in the Hermitian case, $\Re\{(t_L{}^* r_L)\} = 0$, are now coupled through the mediation of the introduced loss.

We can now determine the general criteria for achieving maximal CPA, $\mathcal{A}_T = 1$. From Eq. 2-5, such a goal requires simultaneously satisfying the following conditions:

$$\textit{(I)}\ \ |\boldsymbol{\delta}| = \mathbf{1}\,, \quad \textit{(II)}\ \ \boldsymbol{\cos\theta\cos\phi = -1}\,, \quad \textit{(III)}\ \ |\boldsymbol{r_L}| = |\boldsymbol{t_L}| \qquad (2\text{-}6)$$

$|\delta|$ and ϕ are set by the incident fields, while $\theta, |r_L|, \text{and } |t_L|$ are set by the system characteristics. These conditions correspond in fact to one of the eigenvalues of **S** being zero, signifying a 'dark' eigenstate $\{(output) = \mathbf{S}(input) = (0)(input) = (0)\}$ that is completely absorbed by the system. Condition (II) requires that $(\theta, \emptyset) = (0, \pi) \text{ or } (\theta, \emptyset) = (\pi, 0)$. Condition (III) indicates that a strongly reflecting or transmitting system is not optimal. Instead, we need to arrange for equal reflection and transmission coefficients.

It is crucial to appreciate that the above analysis is independent of any details of the 1D optical system. The conditions in Eq. 2-6 provide a general recipe for constructing a device demonstrating CPA. The typical scenario envisioned is to start from a material or structure that exhibits low intrinsic loss and to then construct around it a *lossless* system that enables CPA. Equation 2-6 may then be used to optimize the CPA effect and reach $\mathcal{A}_T = 1$.

3. MODEL FOR BROADBAND CPA

We now analyze a specific model system to highlight the utility of these results. Figure 3-1 depicts a FP resonator consisting of two mirrors M1 and M2 that sandwich a dielectric layer of thickness *d* and complex refractive index $n + in'$ (positive n' corresponds to loss).

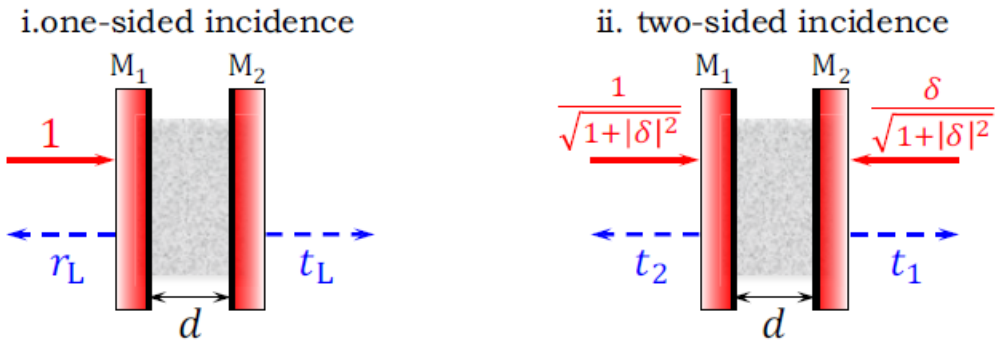

Figure 3-1: Schematic of a symmetric FP cavity formed of mirrors M1 and M2 sandwiching a lossy dielectric. The left and right panels depict the one- and two-sided-incidence configurations, respectively.

3.1. Symmetric FP resonator

The mirrors are identical, lossless but not necessarily symmetric, each has the scattering matrix $\boldsymbol{S_M} = e^{i\beta}\begin{pmatrix} t & -re^{i(\beta-\alpha)} \\ re^{-i(\beta-\alpha)} & t \end{pmatrix}$, $r^2 + t^2 = 1$, α and β are the phases for transmission and reflection from the left, respectively, and the mirrors are arranged to produce a symmetric cavity. **Here $\mathbf{r}$ is the reflection coefficient for incidence from the dielectric layer material**.

The transfer matrix representation of the above arrangement is as follows:

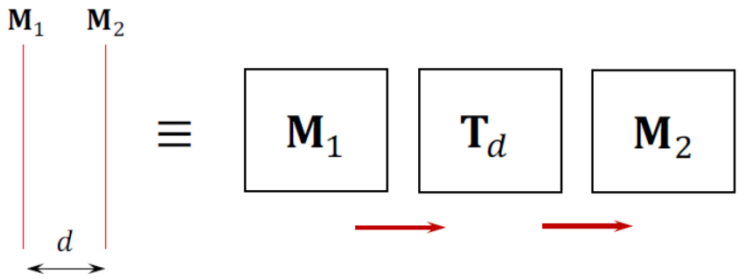

Figure 3-2: Equivalent representation of the FP cavity using transfer matrices

If the complex refractive index of the dielectric layer is $n_{\mathrm{d}} = n + in'$, where the positive sign of the imaginary part n' corresponds to absorption, then the fraction of light absorbed after a single pass in a layer of thickness d is $\boldsymbol{\mathcal{A}} = \mathbf{1} - \boldsymbol{e^{-2k'd}}$, $0 \le \mathcal{A} \le 1$, where $k' = \frac{2\pi}{\lambda}n'$ and λ is the free-space wavelength.

$$\boldsymbol{T} = \boldsymbol{T}_{M1}\boldsymbol{T}_d\boldsymbol{T}_{M2} = \boldsymbol{T}_1'\boldsymbol{T}_d\boldsymbol{T}_1, \quad \boldsymbol{T}_d = \begin{pmatrix} e^{-i\vec{k}d} & 0 \\ 0 & e^{i\vec{k}d} \end{pmatrix}, \quad \vec{\boldsymbol{k}} = \frac{\omega}{c}n - i\frac{\omega}{c}n' = k - ik'$$

$$= \frac{e^{-i2\beta}}{t^2}\begin{pmatrix} 1 & -r\,e^{i\alpha} \\ -r\,e^{i(2\beta-\alpha)} & e^{i2\beta} \end{pmatrix}\begin{pmatrix} e^{k'd-ikd} & 0 \\ 0 & e^{-k'd+ikd} \end{pmatrix}\begin{pmatrix} 1 & r\,e^{i(2\beta-\alpha)} \\ r\,e^{i\alpha} & e^{i2\beta} \end{pmatrix}$$

Obtaining the following components of the total transfer function:

$$t_{11} = \frac{e^{-i2\beta}}{t^2} e^{-ikd}\left\{e^{k'd} - r^2 e^{-k'd} e^{i(2kd+2\alpha)}\right\}$$

$$t_{12} = \frac{e^{-i2\beta}}{t^2} e^{-ikd} e^{i(2\beta-\alpha)}\left\{e^{k'd} - e^{-k'd} e^{i(2kd+2\alpha)}\right\}$$

$$t_{21} = -\frac{e^{-i2\beta}}{t^2} e^{-ikd} e^{i(2\beta-\alpha)}\left\{e^{k'd} - e^{-k'd} e^{i(2kd+2\alpha)}\right\}$$

$$t_{22} = \frac{e^{i2\beta}}{t^2} e^{ikd}\left\{e^{-k'd} - r^2 e^{k'd} e^{-i(2kd+2\alpha)}\right\}$$

Note that $t_{11} \neq t_{22}^*$ and $\det\mathbf{T} \neq 1$.

The scattering elements can now be obtained:

$$t_L = t^2 e^{i(2\beta-\alpha)} \frac{e^{i(kd+2\alpha)}}{e^{k'd} - r^2 e^{-k'd} e^{i(2kd+2\alpha)}} \quad = \quad (1-R) e^{i(2\beta-\alpha)} \frac{e^{i(kd+2\alpha)}}{e^{k'd} - Re^{-k'd} e^{i(2kd+2\alpha)}}$$

$$r_L = -re^{i(2\beta-\alpha)} \frac{e^{k'd} - e^{-k'd} e^{i(2kd+2\alpha)}}{e^{k'd} - r^2 e^{-k'd} e^{i(2kd+2\alpha)}} \quad = \quad -\sqrt{R} e^{i(2\beta-\alpha)} \frac{e^{k'd} - e^{-k'd} e^{i(2kd+2\alpha)}}{e^{k'd} - Re^{-k'd} e^{i(2kd+2\alpha)}}$$

$\mathrm{t_R} = \mathrm{t_L}$, $\mathrm{r_R} = \mathrm{r_L}$, **R is the power reflection for incidence from the dielectric layer material**

The power transmission and reflection are:

$$\mathrm{T_L} = \frac{(1-\mathrm{R})^2}{e^{2k'd} + R^2 e^{-2k'd} - 2R\cos(2kd+2\alpha)}$$

$$\mathrm{R_L} = R\frac{e^{2k'd} + e^{-2k'd} - 2\cos(2kd+2\alpha)}{e^{2k'd} + R^2 e^{-2k'd} - 2R\cos(2kd+2\alpha)}$$

On resonance, we have $2kd + 2\alpha = 2m\pi$, where $m = 1,2,3,\cdots$, and the power reflection and transmission coefficients are

$$T_{\mathrm{L}} = \left(\frac{1-R}{e^{k'd} - Re^{-k'd}}\right)^2, \quad R_{\mathrm{L}} = R\left(\frac{2\sinh k'd}{e^{k'd} - Re^{-k'd}}\right)^2.$$

Due to absorption inside the cavity, $\mathrm{T_L} + \mathrm{R_L} \neq 1$. Instead, $\mathrm{T_L} + \mathrm{R_L} = 1 - \mathcal{A}_L$, where $\mathcal{A}_L$ is the one-sided absorption:

$$\mathcal{A}_L = \mathcal{A}(1-R)\frac{1+R(1-\mathcal{A})}{\{1-R(1-\mathcal{A})\}^2}, \qquad (\boldsymbol{\mathcal{A} = 1 - e^{-2k'd}} \textbf{ = single pass absorption})$$

To find the mirror reflectivity that optimizes $\mathcal{A}_{\mathrm{L}}$, we set $\frac{d\mathcal{A}_{\mathrm{L}}}{dR} = 0$ and solve for

$$R = R^{(1)} = \frac{3 - e^{2k'd}}{3 - e^{-2k'd}} = \frac{2 - 3\mathcal{A}}{(1-\mathcal{A})(2+\mathcal{A})}$$

The optimal **one-sided** absorption is thus $\mathcal{A}_L^{(m)} = \frac{1}{2}\cosh^2 k'd$.

The two-sided absorption coefficient is *(equation 2-5)* :

$\mathcal{A}_T = \mathcal{A}_L - \frac{4|\delta|}{1+|\delta|^2}\Re\{(t_L{}^* r_L)\}\, cos\, \emptyset$

On resonance when $|a| = |b| = \frac{1}{\sqrt{2}}$, $(|\delta| = 1)$, $\mathcal{A}_T$ is given by

$$\mathcal{A}_T = \mathcal{A}_{\mathrm{L}} + 2(-1)^m \cos\emptyset \frac{\mathcal{A}(1-R)\sqrt{R(1-\mathcal{A})}}{\{1-R(1-\mathcal{A})\}^2}$$

If we set $\emptyset = 0$ or π, then $(-1)^m \cos\emptyset = \pm 1$, and $\mathcal{A}_{\mathrm{T}}$ becomes

$$\mathcal{A}_{\mathrm{T}} = \mathcal{A}(1-R)\left\{\frac{1 \pm \sqrt{R(1-\mathcal{A})}}{1-R(1-\mathcal{A})}\right\}^2$$

To optimize $\mathcal{A}_{\mathrm{T}}$, we set $\frac{d\mathcal{A}_{\mathrm{T}}}{dR} = 0$ and solve for

$R = R^{(2)} = e^{-2k'd} = 1 - \mathcal{A}$,

upon which the optimal **two-sided** absorption is $\mathcal{A}_T^{(m)} = \frac{1 \pm (1-\mathcal{A})}{2-\mathcal{A}}$.

The plus sign (corresponding to only half of the resonances, of either even or odd order) results in the 'dark state' $\mathcal{A}_{\mathrm{T}} = 1$ and CPA is achieved. The negative sign (corresponding to the other half of the resonances) results in $\mathcal{A}_{\mathrm{T}} = \frac{\mathcal{A}}{2-\mathcal{A}} = \tanh k'd$, which is the remnant absorption in the 'bright state'. When $R = R^{(2)}$, one-sided absorption is sub-optimal at $\mathcal{A}_{\mathrm{L}} = 1 - \frac{1}{2}\mathrm{sech}^2\, k'd$.

Disregarding dispersion in R , n and n' , Figure 3-3 illustrates transmission and reflection resonances for the first four resonance orders for one-sided and two-sided incidence.

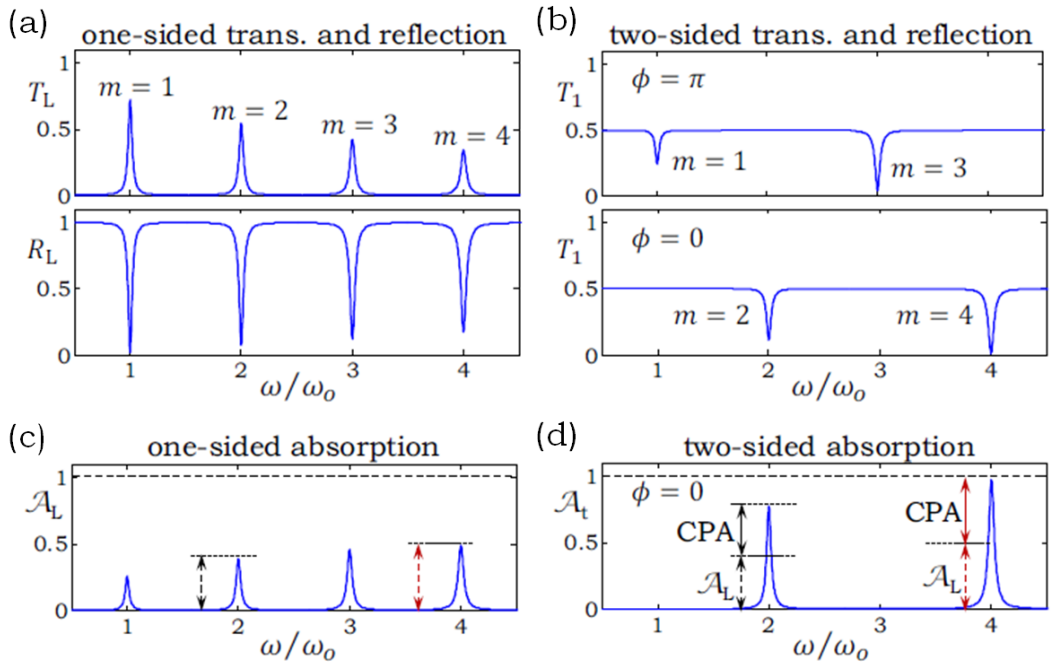

Figure 3-3: (a) One-sided transmission T_L and reflection R_L coefficients against normalized frequency showing the first four resonances; $\omega_0 = \frac{\pi c}{nd}$, m is the resonance order , n' = 0.003, and R = 0.9. (b) Two-sided transmission T_1 , with $|\delta| = 1$. Top and bottom panels show T_1 for ϕ = π (achieving CPA for odd-m resonances) and ϕ = 0 (for even-m resonances), respectively. The results for T_2 in both cases are identical to T_1 since the system is symmetric. (c) One-sided absorption $\mathcal{A}_L = 1 - \{T_L + R_L\}$. The height of the two resonances m = 2, 4 are highlighted for reference. (d) Two-sided absorption $\mathcal{A}_T = 1 - \{T_1 + T_2\}$. The contributions of $\mathcal{A}_L$ (dashed arrows) and CPA (solid arrows) to the m = 2 and m=4 resonances are highlighted.

Increasing the intrinsic losses $k'd$ does *not* necessarily increase $\mathcal{A}_L$. Surprisingly, *increasing* n' indefinitely *decreases* absorption. The reason is that light transmitted through M_1 fails to reach M_2, thereby disrupting the FP interference. Consequently, the reflected fraction $R_L \approx R$ of light from M_1 remains undiminished and $\mathcal{A}_L \to 1 - R \approx 0$. This result suggests the following question: for a given value of $k'd$ (especially $k'd \ll 1$), what is the *maximum* one-

sided absorption $\mathcal{A}_L^{(m)}$ that may be achieved in this structure?

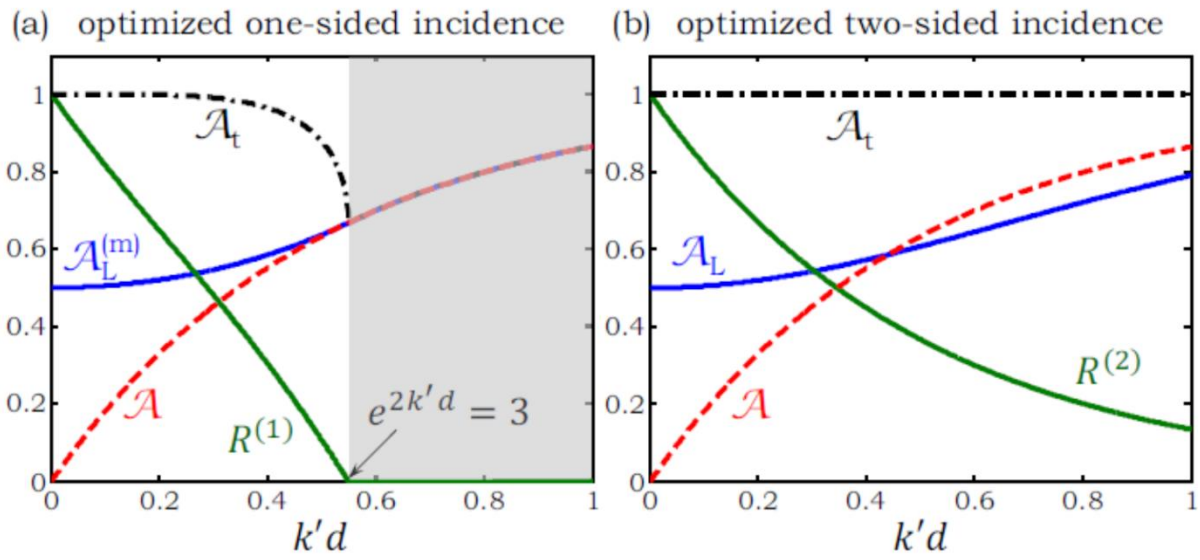

Figure 3-4: (a) The maximal one-sided absorption $\mathcal{A}_L^{(m)}$ and optimal mirror reflectivity $R^{(1)}$ that produces it for a given value of $k'd$. The dashed red curve $\mathcal{A}$ corresponds to the single-pass absorption $1 - e^{-2k'd}$. The shaded region corresponds to $e^{2k'd} > 3$, a regime in which it is optimal to set $R^{(1)} = 0$, resulting in $\mathcal{A}_L^{(m)} = \mathcal{A}_T = \mathcal{A}$. (b) The maximal two-sided absorption $\mathcal{A}_t = 1$ (CPA), the optimal mirror reflectivity $R^{(2)}$ that produces it for a given value of $k'd$, and the corresponding $\mathcal{A}_L$.

It was shown above that $\mathcal{A}_L^{(m)} = \frac{1}{2}cosh^2 k'd \geq \frac{1}{2}$ on resonance when mirrors having dispersive reflectivity $R^{(1)} = \frac{3-e^{2k'd}}{3-e^{-2k'd}}$ are used – a condition that applies only when $e^{2k'd} < 3$ [Fig. 3-4(a)], or equivalently $0 < \mathcal{A} \leq \frac{2}{3}$, at the end of which $\mathcal{A}_L = \mathcal{A} = \frac{2}{3}$. Therefore, even in the limit $k'd \ll 1$, one may still achieve *at least* 50% absorption on resonance, no matter how low the intrinsic absorption $\mathcal{A}$ is. As $k'd$ increases, the mirror reflectivity needed to optimize one-sided absorption decreases. When $e^{2k'd} < 3$, the optimal one-sided absorption $\mathcal{A}_L^{(m)} = 1 - e^{-2k'd}$ is achieved with $R^{(1)} = 0$; that is, adding the mirrors does not improve the absorption above that of a single pass.

Consider now *two*-sided incidence [Fig. 3-1(ii); $|\delta| = 1$] where the total absorption $\mathcal{A}_T$ [Eq. 2-5] is the sum of $\mathcal{A}_L$ [Eq. 2-3] and an absorption-mediated interference term:

$$-2\Re\{({t_L}^* r_L)\} = \frac{4\sqrt{R}}{1-R}(-1)^m T_L \sinh k'd \qquad (3\text{-}1)$$

where *m* = 1, 2, . . . is the resonance order, resulting in either even-*m* or odd-*m* resonances having enhanced absorption [Fig. 3-3(d)]. It is straightforward to show that maximal CPA [Eq. 3-1] is achieved on resonance when $R^{(2)} = e^{-2k'd} = 1 - \mathcal{A}$. However, this choice for $R^{(2)}$ does *not* maximize $\mathcal{A}_L = 1 - \frac{1}{2}sech^2 k'd \leq \mathcal{A}_L^{(m)}$ for a given $k'd$, as shown in Fig. 3-4(a), but it does ensure that $\mathcal{A}_T = 1$. Finally, note that for $k'd \ll 1$, $R^{(1)} \approx R^{(2)} \approx 1 - 2k'd$, so that the same mirror simultaneously optimizes $\mathcal{A}_L$ and $\mathcal{A}_T$.

3.2. Asymmetric FP resonator

Instead of using two beams coupled to the two inputs of a symmetric FP cavity, coherent perfect absorption may be realized in an asymmetric FP cavity with a perfect second mirror.

Referring to Figure 3-1, we consider now the case of a FP cavity with two different mirrors,

$$\mathbf{T} = \mathbf{T}_{\mathrm{M1}^{(a)}}\mathbf{T}_{\mathrm{d}}\mathbf{T}_{\mathrm{M2}^{(a)}} = \mathbf{T}_1'\mathbf{T}_{\mathrm{d}}\mathbf{T}_2$$

$$= \frac{e^{-i(\beta_1+\beta_2)}}{t_1 t_2}\begin{pmatrix} 1 & -r_1\, e^{i\alpha_1} \\ -r_1\, e^{i(2\beta_1-\alpha_1)} & e^{i2\beta_1} \end{pmatrix}\begin{pmatrix} e^{k'd-ikd} & 0 \\ 0 & e^{-k'd+ikd} \end{pmatrix}\begin{pmatrix} 1 & r_2\, e^{i(2\beta_2-\alpha_2)} \\ r_2\, e^{i\alpha_2} & e^{i2\beta_2} \end{pmatrix}$$

Where r_1 and r_2 are the reflection coefficients for incidence from the dielectric layer material.

Obtaining the following components of the total transfer function:

$$t_{11} = \frac{e^{-i(\beta_1+\beta_2)}}{t_1 t_2} e^{-ikd}\left\{e^{k'd} - r_1 r_2 e^{-k'd} e^{i(2kd+\alpha_1+\alpha_2)}\right\}$$

$$t_{12} = \frac{e^{-i(\beta_1+\beta_2)}}{t_1 t_2} e^{-ikd} e^{i(2\beta_2-\alpha_2)}\left\{r_2 e^{k'd} - r_1 e^{-k'd} e^{i(2kd+\alpha_1+\alpha_2)}\right\}$$

$$t_{21} = \frac{e^{-i(\beta_1+\beta_2)}}{t_1 t_2} e^{-ikd} e^{i(2\beta_1-\alpha_1)}\left\{-r_1 e^{k'd} + r_2 e^{-k'd} e^{i(2kd+\alpha_1+\alpha_2)}\right\}$$

$$t_{22} = \frac{e^{i(\beta_1+\beta_2)}}{t_1 t_2} e^{ikd}\left\{e^{-k'd} - r_1 r_2 e^{k'd} e^{-i(2kd+\alpha_1+\alpha_2)}\right\}$$

Note that $t_{11} \neq t_{22}^*$ and $\det\mathbf{T} \neq 1$.

The amplitude transmission and reflection coefficients are then given by:

$$t_L = t_1 t_2 e^{i(\beta_1+\beta_2)} \frac{e^{ikd}}{e^{k'd} - r_1 r_2 e^{-k'd} e^{i(2kd+\alpha_1+\alpha_2)}}$$

$$r_L = e^{i(2\beta_1-\alpha_1)} \frac{-r_1 e^{k'd} + r_2 e^{-k'd} e^{i(2kd+\alpha_1+\alpha_2)}}{\mathrm{e}^{\mathrm{k'd}} - r_1 r_2 \mathrm{e}^{-\mathrm{k'd}} e^{i(2kd+\alpha_1+\alpha_2)}}$$

$$r_R = e^{i(2\beta_2-\alpha_2)} \frac{r_2 e^{k'd} - r_1 e^{-k'd} e^{i(2kd+\alpha_1+\alpha_2)}}{\mathrm{e}^{\mathrm{k'd}} - r_1 r_2 \mathrm{e}^{-\mathrm{k'd}} e^{i(2kd+\alpha_1+\alpha_2)}}$$

$M_2^{(a)}$ is perfect mirror $\rightarrow$ $t_2 = 0,\ |r_2| = 1$

The power transmission and reflection coefficients are given by:

$$\mathrm{T_L} = 0$$

$$\mathrm{R_L} = \frac{R_1 e^{2k'd} + e^{-2k'd} - 2\sqrt{R_1}\cos(2kd + \alpha_1 + \alpha_2)}{\mathrm{e^{2k'd}} + R_1 \mathrm{e^{-2k'd}} - 2\sqrt{R_1}\cos(2kd + \alpha_1 + \alpha_2)}$$

$$\mathrm{R_R} = 1$$

On resonance, we have $2kd + \alpha_1 + \alpha_2 = 2m\pi$, where $m = 1,2,3,\cdots$, and the power reflection and transmission coefficients are

$$\mathrm{T_L} = 0$$

$$\mathrm{R_L} = \frac{R_1 e^{2k'd} + e^{-2k'd} - 2\sqrt{R_1}}{\mathrm{e^{2k'd}} + R_1 \mathrm{e^{-2k'd}} - 2\sqrt{R_1}} = \left(\frac{\sqrt{R_1} e^{k'd} - e^{-k'd}}{\mathrm{e^{k'd}} - \sqrt{R_1}\mathrm{e^{-k'd}}}\right)^2$$

Due to absorption inside the cavity, $\mathrm{T_L} + \mathrm{R_L} \neq 1$. Instead, $\mathrm{T_L} + \mathrm{R_L} = 1 - \mathcal{A}_L$, where $\mathcal{A}_L$ is the one-sided absorption ($R = R_1$) :

$$\mathcal{A}_L = \mathcal{A}(1 - R)\frac{(2 - \mathcal{A})}{\{1 - \sqrt{R}(1 - \mathcal{A})\}^2}, \qquad (\mathcal{A} = 1 - e^{-2k'd} = \text{ single pass absorption})$$

To find the mirror reflectivity that optimizes $\mathcal{A}_\mathrm{L}$, we set $\frac{d\mathcal{A}_\mathrm{L}}{dR} = 0$ and solve for

$$R = R^{(1)} = (1 - \mathcal{A})^2$$

The optimal **one-sided** absorption is thus $\mathcal{A}_L^{(m)} = 1$.

4. MULTILAYER MIRROR COMPUTATIONAL MODEL FOR NEAR-INFRARED CPA

After examining the idealized system illustrated in Fig. 3-3 in which we ignored dispersion in R , n and n', we now proceed to a more detailed model consisting of two symmetric multilayer mirrors sandwiching a layer of silicon (Si). While Si has high optical absorption in the visible, its absorption drops rapidly in the infrared. Using the analysis established above, we consider here whether we can achieve CPA in a $1\mu m$-thick layer of Si in the vicinity of $\lambda = 1\mu m$ where Si is only weakly absorbing and the single-pass absorption is $1 - e^{-2k'd} = 0.0064$ using the optical parameters for Si in Ref. [13].

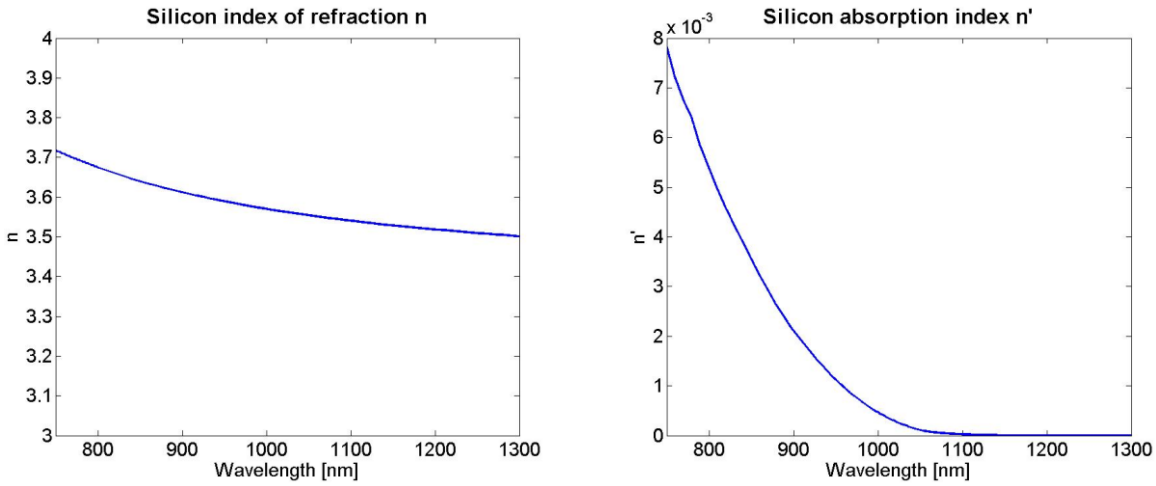

Figure 4-1: Optical parameters for Silicon.

We sandwich the Si thin layer between two Bragg mirrors [Fig. 4-2(b), inset] each formed of 7 bilayers of SiO2 and TiO2 with refractive indices of 1.45 and 2.46 and thicknesses 172.4 and 101.6 nm, respectively [Fig. 4-2(a)], chosen such that the center of the bandgap is at $\lambda = 1\mu m$ [Fig. 4-2(b)] and the total device thickness is $< 5\mu m$. In Fig. 4-2(c) we plot the spectral dependence of four relevant quantities for the full structure: the transmission T_L, reflection R_L, and absorption $\mathcal{A}_L$ for incidence from the left, and the two-sided absorption $\mathcal{A}_t$

for two beams with $|\delta| = 1$. Since R is approximately equal at all resonances within the band but $2k'd$ drops rapidly in Si at longer wavelengths, $\mathcal{A}_L < 0.5$ and $\mathcal{A}_t < 1$.

The strategy to remedy this situation is clear: replace the Bragg mirrors with others whose reflection is low at the shorter wavelengths (where absorption in Si is higher) and high at longer wavelengths (where absorption in Si drops). To optimize CPA in Si, a mirror with dispersive reflection $R = e^{-2k'd}$ is required to replace the Bragg mirror. A design for such a mirror (obtained using the package FilmStar, FTG Software) is shown in Fig. 4-2(d) consisting of 22 alternating layers of SiO2 and TiO2. This mirror's reflection R, assuming left incidence from air and a Si substrate on the right, is shown in Fig. 4-2(e), compared to the ideal target $R = e^{-2k'd}$. By sandwiching a $1\mu m$-thick Si film between two such mirrors symmetrically (total device thickness is <7.9 μm), we now obtain a structure in which complete CPA is achieved within the spectral range where the designed R approaches the ideal target. We plot in Fig. 4-2(f) $T_L, R_L, \mathcal{A}_L,$ and $\mathcal{A}_t$ for this structure, and we confirm that CPA is indeed achieved within the spectral range 750 – 1000 nm. Noteworthy is the dramatically increased number of resonances with complete CPA for both one-sided and two-sided incidence. A subtle effect must be stressed here. As shown in Fig. 4-2(f), $\mathcal{A}_{\mathrm{L}} \geq \frac{1}{2}$ occurs for *all* the resonances when $R = R^{(1)}$. When $R = R^{(2)}$ (here $R^{(2)} \approx R^{(1)}$), however, we achieve $\mathcal{A}_{\mathrm{t}} = 1$ at only *half* the resonances since $\mathcal{A}_{\mathrm{t}} = 1 - \frac{1}{2}\{1 - (-1)^m \cos\varphi\}\,\mathrm{sech}^2\, k'd$, where m is the resonance order (see Chapter 3.1). This feature is not important when a single resonance is targeted, since we can always achieve $\mathcal{A}_2 = 1$ and $\mathcal{A}_1 \geq \frac{1}{2}$ at a single wavelength simultaneously. However, when a *broad bandwidth* is of interest, this result indicates, surprisingly, that one-sided incidence in a

symmetric structure yields a larger *total* absorption than two-sided incidence – with no need to arrange for the interference of two beams. This feature is particularly interesting since it offers experimental simplification and also facilitates the use of incoherent light.

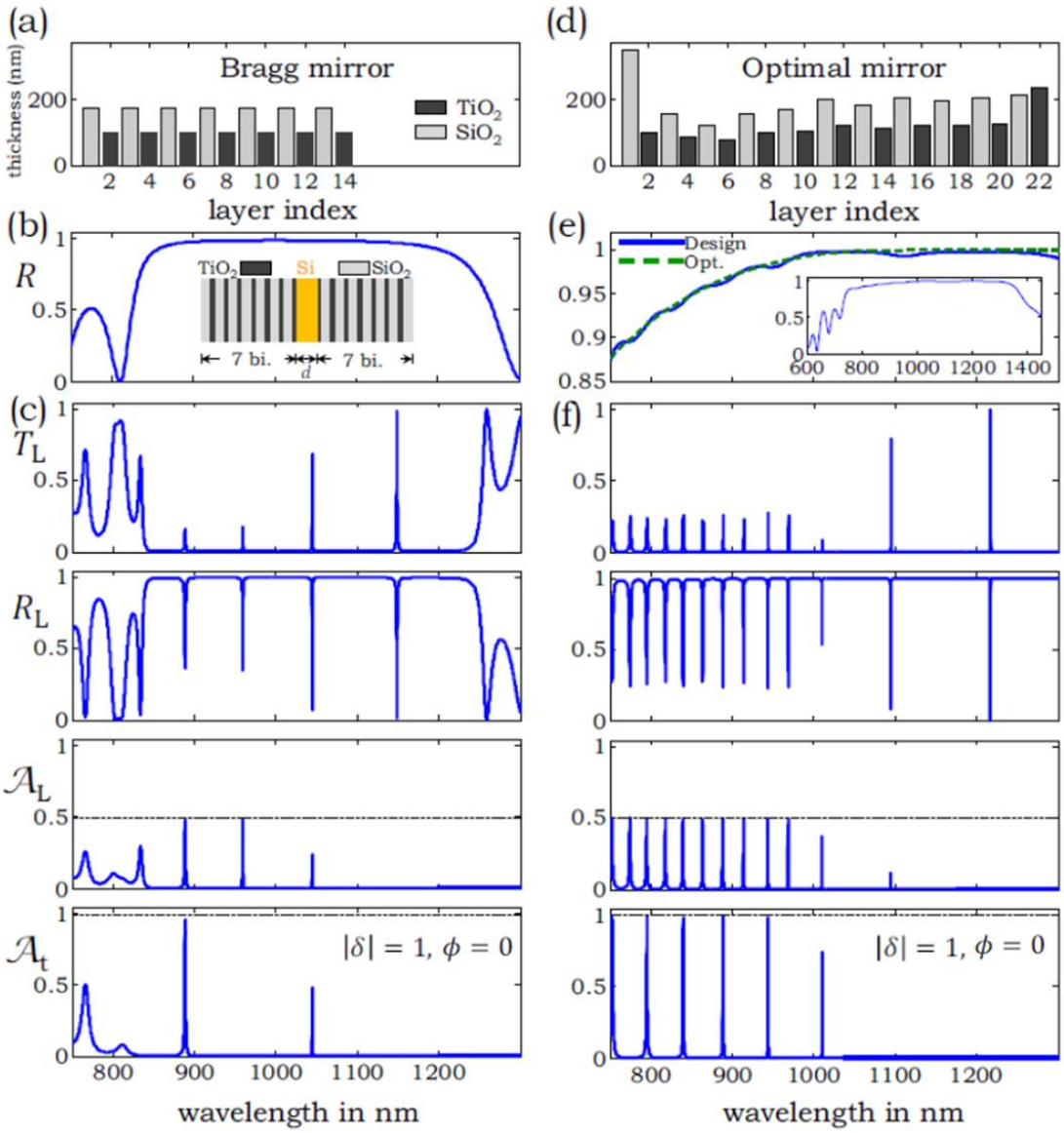

Figure 4-2: (a) Layer thicknesses of a 7-bilayer Bragg mirror with central wavelength 1 µm. (b) Reflection of the mirror in (a). Inset is a schematic of the overall structure under consideration; d=1 µm. (c) The four panels from top to bottom correspond to the one-sided transmission TL, reflection RL, absorption AL, and two-sided absorption At, respectively. (d) Layer thicknesses of a mirror designed to optimize CPA in Si in the near-infrared. (e) Reflection of the mirror in (d), compared to the ideal design, assuming incidence from air from the left and a Si substrate on the right. Inset shows R on a wider spectral range. (f) Same as in (c) with the mirror in (d) replacing the Bragg mirror.

In this chapter we have presented a general model for CPA in 1D photonic structures that establishes the general criteria for achieving maximal CPA. On this understanding, CPA is an absorption-mediated interference effect that is normally forbidden in lossless systems, but is allowed when conservation of energy is violated due to the inclusion of loss. Using this recipe we have demonstrated that one may optimize near-infrared CPA in a thin silicon film placed in a planar cavity. CPA is achieved in this lossy Fabry-Pérot cavity model *only* at its resonance frequencies. *Continuous broadband* CPA, which would have important applications in solar energy for example, cannot be accomplished with these means, and further research is necessary to identify suitable mechanisms and structures for its demonstration. A promising approach is described in Chapter 6.

5. MULTILAYER MIRROR REALIZATION FOR NEAR-INFRARED CPA

We apply here the theory and methods derived in the previous chapters and show experimentally that judicious engineering of the photonic environment of a thin film severs the link between the effective optical absorption of the film and the intrinsic absorption of its material. Using few-micron-thick aperiodic planar dielectric mirrors [Fig. 5-1], we demonstrate spectrally flat, coherently enhanced absorption at the theoretical limit in a 2-micron-thick film of polycrystalline silicon embedded in symmetric and asymmetric cavities. The material presented in this chapter was developed as a team effort in the context of an article soon to be submitted for publication in a major scientific journal [35].

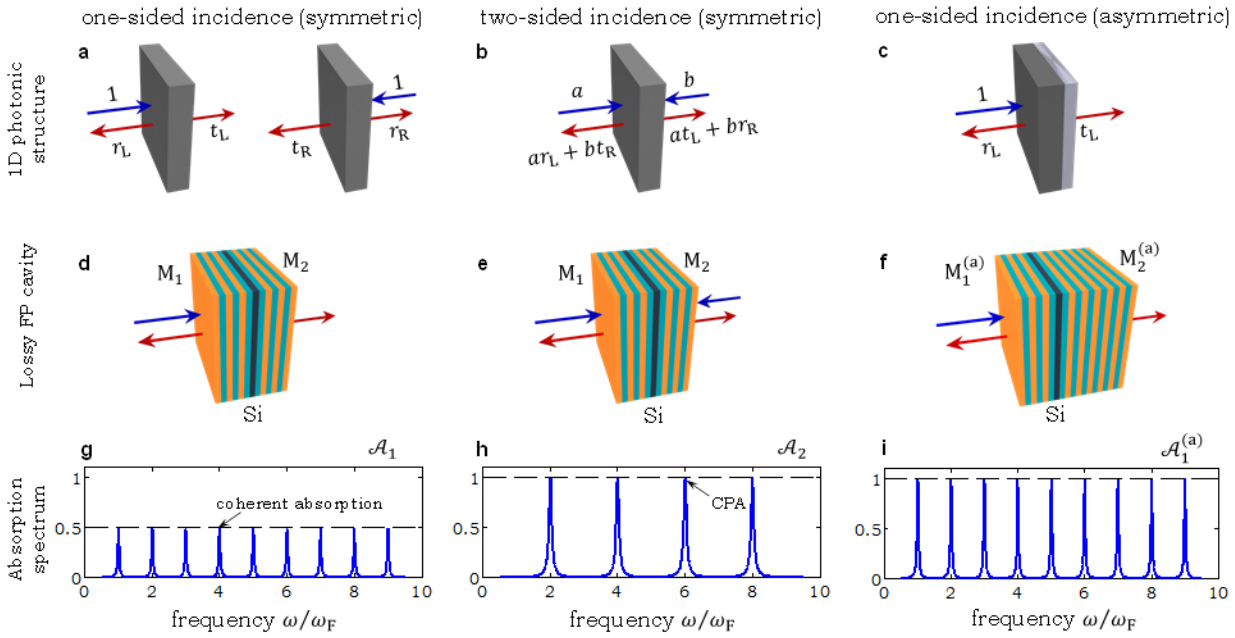

Figure 5-1: (a) Left and right one-sided incidence on a generic 1D photonic structure (depicted as a slab). Here r_L and t_L are the field reflection and transmission coefficients for left incidence, and r_R and t_R are the corresponding quantities for right incidence. (b) Two-sided incidence on a symmetric 1D structure. (c) One-sided incidence on an asymmetric 1D structure. (d) One- and (e) two-sided incidence on a symmetric 1D cavity consisting of a thin film of Si between two multilayer dielectric mirrors M_1 and M_2 (which has reversed-layer order). (f) One-sided incidence on an asymmetric 1D cavity consisting of a thin film of Si between mirror $M_1^{(a)}$ and $M_2^{(a)}$. (g) One-sided absorption $\mathcal{A}_1(\lambda)$ for the symmetric device in (d) with ideal mirrors; $\mathcal{A}_1 = \frac{1}{2}$ at all the resonances; ω is frequency and ω_F is the frequency spacing of the cavity modes. (h) Two-sided absorption $\mathcal{A}_2(\lambda)$ for the symmetric device in (e) with ideal mirrors; $\mathcal{A}_2 = 1$ at only half the resonances and $\mathcal{A}_2 = 0$ at the other half. Here, the two incident fields are equal in amplitude and have a fixed phase relationship. (i) One-sided absorption $\mathcal{A}_1^{(a)}$ for the asymmetric device in (f) with ideal front mirror $M_1^{(a)}$ and unity-reflection back mirror $M_2^{(a)}$. Here, $\mathcal{A}_1^{(a)} = 1$ at all the resonances.

Inverse mirror design

We carried out the inverse design of the target mirror in a symmetric device $R_2(\lambda) = 1 - \mathcal{A}(\lambda)$ (Fig. 5-2c) to optimize two-sided absorption, and simultaneously one-sided absorption for low $\mathcal{A}$ (Fig. 5-2a), using the FilmStar software package (FTG Software Associates). This software employs damped least-squares optimization to inversely synthesize the structure through computing the derivatives (differential change in layer thickness) at each target reflectivity point over the spectrum and iterative matrix inversion [20, 28]. Using lossless materials with indices $n_{\mathrm{L}} = 1.5$ and $n_{\mathrm{H}} = 2.45$, we optimized the structure design iteratively while reducing the number of layers N, to simplify fabrication and reduce the structure thickness. Employing $N = 13$ layers for the mirrors M_1 and M_2 in a symmetric structure, with the sequence of thicknesses shown in Fig. 5-5a, the resulting mirror has a reflectivity that approaches the target over an octave of bandwidth in the NIR, $\sim 800 - 1600$ nm [Fig. 5-5b]. The thickness of this mirror is ≈ 2.2 μm, resulting in a total device thickness of $\approx 2 \times 2.2 + 2 = 6.4$ μm. In contrast to the Bragg condition, where the ratio of the layer thicknesses is in inverse proportion to the ratio of their refractive indices, some of the high-refractive-index layers in our mirror design are in fact thicker than some of their low-refractive-index counterparts. Allowing for more layers N, and consequently a thicker device, enables more accurate approximation to the desired target spectral reflectivity $R(\lambda)$. The question of the robustness of this effect with respect to finite fabrication tolerances in the construction of M_1 compared to the ideal design naturally arises. We present in Chapter 5.3. a quantitative study of the impact of relative and absolute errors in layer thicknesses on $R(\lambda)$, and the effect of deviations in $R(\lambda)$ from the target design on $\mathcal{A}_2$.

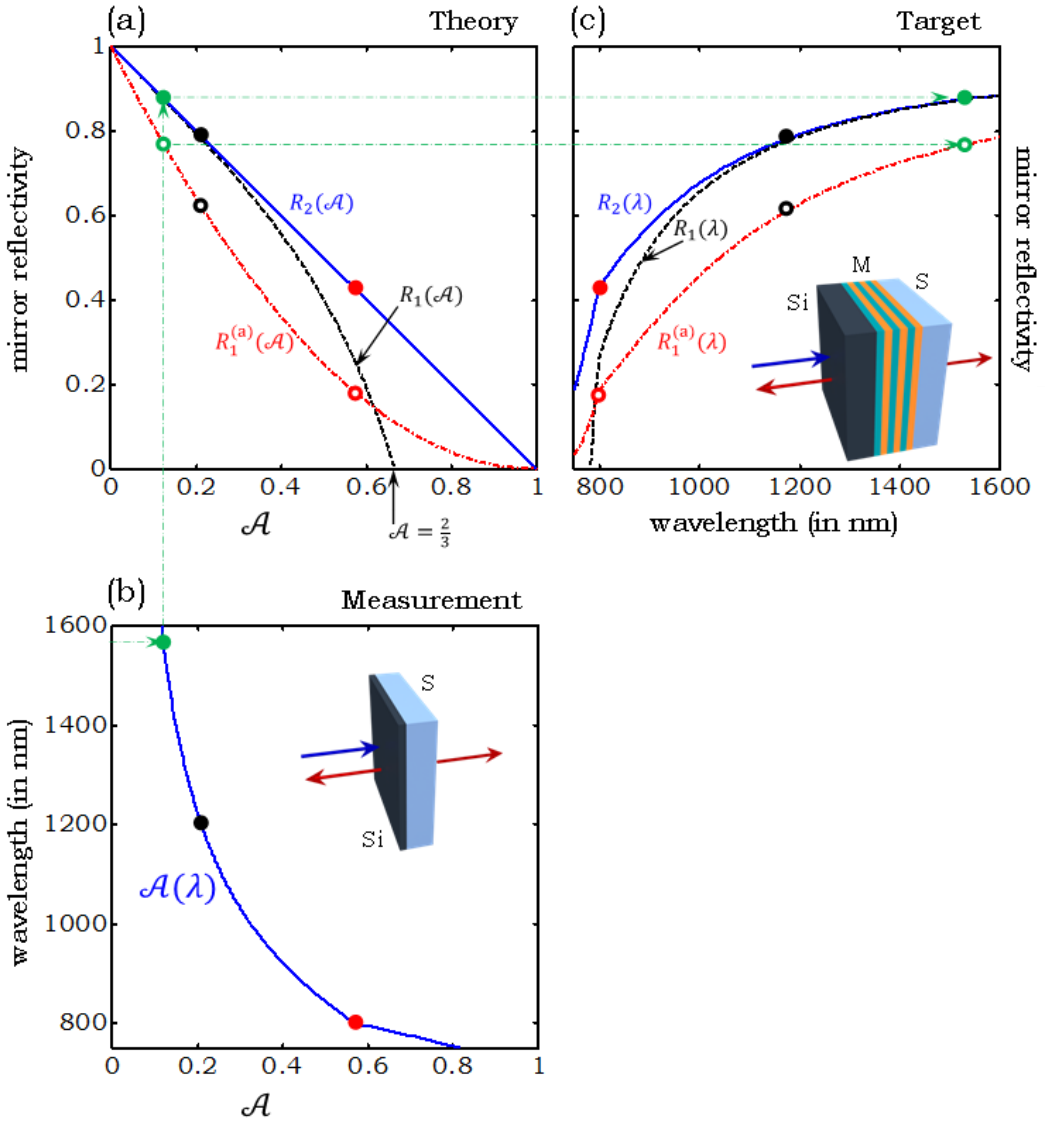

Figure 5-2: Ideal mirror reflectivity to optimize one- and two-sided coherent absorption. (a) Theoretical model for mirror reflectivities R_1 and R_2 in a symmetric cavity for optimal one- and two-sided absorption $\mathcal{A}_1$ (Fig. 5-1d) and $\mathcal{A}_2$ (Fig. 5-1e), respectively, and $R_1^{(a)}$ for optimal one-sided absorption $\mathcal{A}_1^{(a)}$ in an asymmetric cavity (Fig. 5-1f) – all versus single-pass absorption $\mathcal{A}$. We highlight $\mathcal{A}=\frac{2}{3}$, the limit for coherent enhancement of absorption for one-sided incidence in a symmetric cavity. (b) Measured single-pass absorption $\mathcal{A}$ in a 2-μm-thick layer of polycrystalline Si on a glass substrate (S) obtained by spectroscopic ellipsometry. The plot is rotated such that wavelength is the vertical axis to align the horizontal axes in (a) and (b), both corresponding to $\mathcal{A}$. (c)Targeted $R_1(\lambda)$, $R_2(\lambda)$, and $R_1^{(a)}(\lambda)$ to optimize $\mathcal{A}_1$, $\mathcal{A}_2$, and $\mathcal{A}_1^{(a)}$ in the Si layer in (b), respectively. The mirror is on a glass substrate (S) and light is incident from Si. Insets in (b) and (c) show the corresponding configurations schematically. Three equally spaced wavelengths are selected in (b), from 800 nm to 1600 nm, and shown as solid or hollow colored circles for $\mathcal{A}_2$, and $\mathcal{A}_1^{(a)}$ in the three panels, respectively. Dashed-dotted arrows are aids for the eye in conveying the transformation from measured absorption to target mirror reflectivity.

For asymmetric configurations, we designed a mirror $\mathrm{M}_1^{(\mathrm{a})}$ having reflectivity $\mathrm{R}_1^{(\mathrm{a})}(\lambda) = [1 - \mathcal{A}(\lambda)]^2$ (Fig. 5-7a-f) and a back reflector $\mathrm{M}_2^{(\mathrm{a})}$ having flat unity-reflectivity over the bandwidth octave of interest (Fig. 5-7d-f). In this design, $\mathrm{M}_1^{(\mathrm{a})}$ ($\mathrm{M}_2^{(\mathrm{a})}$) consists of 14 (30) alternating layers of materials with indices $\mathrm{n_L} = 1.5$ and $\mathrm{n_H} = 2.45$ and total thickness of 1.8 μm (4.5 μm). The total asymmetric device thickness is 8.3 μm. The sequences of layer thicknesses for both mirrors are given in Fig. 5-7. Note that in both the symmetric and asymmetric devices, the thicknesses of the mirrors are on the order of the thickness of the Si layer itself, and they may be further reduced using higher-index-contrast materials [29].

Optical characterization of the polycrystalline Si used

Since the evaporated layer of polycrystalline Si is a critical component of the full devices examined in this Chapter, whether symmetric or asymmetric, we present here the results of optical measurements of such a film on a glass substrate. We have measured the complex refractive index through spectroscopic ellipsometry (Fig. 5-3a,b), from which we estimate the absorption and thus the transmission through such a film (Fig. 5-3c). These results are then confirmed by direct measurement of thin-film transmission (Fig. 5-3d).

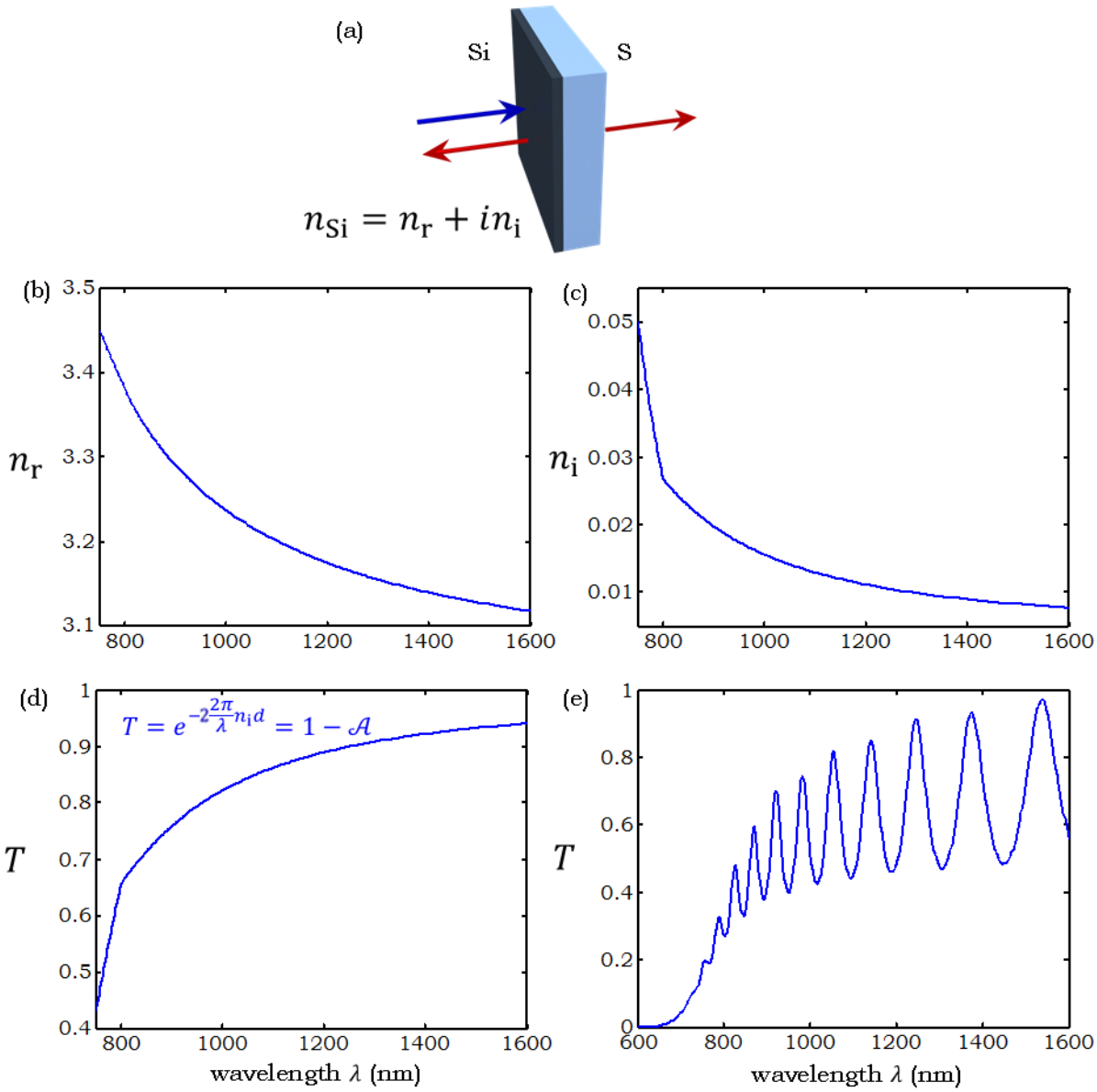

Figure 5-3: *Spectral measurements for Si. (a) Schematic of the Si layer on a glass substrate (S). (b) Measurement of n_r and (c) n_i versus wavelength obtained from spectroscopic ellipsometry measurements. (d) Calculated optical spectral transmission $T(\lambda)$ through a 2-µm-thick Si layer estimated from $T = e^{-2\frac{2\pi}{\lambda}n_i d}$ with the measured n_i in (c), $d = 2$ µm, and λ is the wavelength. Note that $\mathcal{A} = 1 - T$ was used in designing the mirrors in Fig. 5-5 / Chapter 5.1. below. (e) Optical spectral transmission $T(\lambda)$ through a 2-µm-thick Si layer on a glass substrate showing the resonances in the thin Si film.*

Device fabrication.

The full symmetric device structure (M_1 + Si film + M_2) was fabricated sequentially using physical vapor deposition employing as high- and low-refractive-index dielectrics ZnSe ($n_{\mathrm{H}} = 2.45$) and ThF_4 ($n_{\mathrm{L}} = 1.5$), respectively. First, alternating ZnSe and ThF_4 layers are deposited from resistive targets on BK7 substrates (refractive index $n_{\mathrm{s}} = 1.52$) to form M_1; a 2-µm-thick polycrystalline Si layer is added via e-beam evaporation; and, finally, M_2 is deposited with the reverse layer-order of M_1. With the addition of a 1-mm-thick borosilicate glass slide after M_2, we obtain a symmetric structure. This fabrication sequence allowed us to isolate the individual components that constitute the structure, the mirrors M_1 and M_2 and the Si layer, for characterization. The measured spectral reflection and transmission from M_1 (on the BK7 substrate) compared to transfer-matrix calculations is shown in Fig. 5-4c. Note that incidence is from air in Fig. 5-5c, and not from Si as in Fig. 5-5b, which dramatically changes the spectral reflection from this mirror.

A similar approach was followed to fabricate and characterize the asymmetric device ($\mathrm{M}_1^{(\mathrm{a})}$ + Si film + $\mathrm{M}_2^{(\mathrm{a})}$). Mirror $\mathrm{M}_1^{(\mathrm{a})}$ was designed assuming incidence from air, and no extra glass slide is required here. Measurements for $\mathrm{M}_1^{(\mathrm{a})}$ and $\mathrm{M}_2^{(\mathrm{a})}$ corresponding to those of M_1 in Fig. 5-5a-c are presented in Fig. 5-8a-c and Fig. 5-8d-f, respectively.

Thin-film deposition process for device fabrication

The coatings for the ZnSe/ThF_4 multi-layer mirrors and the Si dielectric sandwiched between them were fabricated at Quality Thin Films (QTF, Oldsmar, FL, USA). The coatings were deposited using a combination of two vacuum chambers, both pumped to the desired

environment using cryogenic pumps, typically a vacuum environment achieving a base nominal pressure of 5×10^{-6} torr. Coating processes were of the physical vapor deposition (PVD) type, using a combination of technologies: e-beam for Si (VPT Technologies VPT # 3000 GPOC - 30 inch square vacuum chamber) and thermal evaporation resistive sources for ZnSe/ThF_4 (DW Industries DW-3 #21750 - 32 inch diameter steel bell jar vacuum chamber). Substrates were prepared in a class-1000 clean room under class 100 HEPA filter flow.

Symmetric device: Starting from a BK7 substrate (25-mm-diameter, 3.2-mm-thick), the sequence of layers shown in Fig. 5-5a is evaporated to produce mirror M_1. Some samples are removed from the chamber at this stage (and used to obtain the spectral reflectivity $R(\lambda)$ shown in Fig. 5-5c) and replaced with fresh substrates. The Si layer is evaporated, resulting in S+M_1+Si and S+Si layers, the latter of which are used to obtain the spectral single-pass absorption curve $\mathcal{A}(\lambda)$ in Fig. 5-3d]. Some samples are removed from the chamber at this stage. Finally, the reversed sequence of layers shown in Fig. 5-5a is evaporated to produce mirror M_2, resulting in S+M_1+Si+M_2, and S+M_2 structures. To render the full structure symmetric, a borosilicate slide (1-mm-thick) is placed on the final structure S+M_1+Si+M_2+S.

Asymmetric device: A similar process was used as described above for the symmetric device, however starting with the deposition of mirror $\mathrm{M}_2^{(\mathrm{a})}$ on BK7 substrate, since the design assumed incidence from air on mirror $\mathrm{M}_1^{(\mathrm{a})}$.

One-sided absorption measurements

Light from a Tungsten lamp (Thorlabs QTH10; 50 mW, spectrum given in Fig. 5-4) is coupled into a multimode fiber (50-µm-diameter core) using an achromatic doublet lens L_1 with focal length

$f = 4$ cm. Light exiting the fiber is collimated via a $f = 8$ mm aspheric lens L_2 to a 2-mm-diameter beam incident normally on the samples after traversing a 50/50 plate beam splitter used to avoid multiple reflections that may occur in a cube beam splitter.

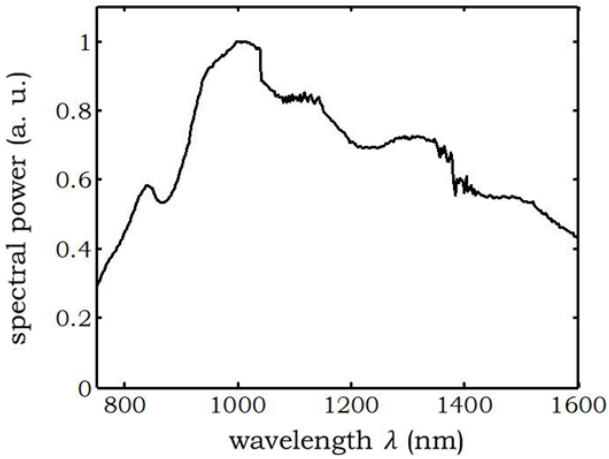

Figure 5-4: Spectrum of the tungsten source used in the device measurements.

The spectrum of the transmitted beam $T_{\text{sample}}(\lambda)$ is coupled via an achromatic doublet lens L_3 with focal length $f = 3$ cm to a 50-µm-diameter fiber and measured with an optical spectrum analyzer, OSA (Advantest Q8381 A) at a resolution of 2 nm. The transmitted beam is normalized with respect to the beam detected when the sample is removed from the optical path, $T_{\text{ref}}(\lambda)$. The reflected beam is coupled to the OSA in the same way as the transmitted beam. The beam reflected from the sample $R_{\text{sample}}(\lambda)$ is normalized with respect to the beam reflected from a protected silver mirror $R_{\text{ref}}(\lambda)$ (Melles Griot, 02MPG-007/038; Thorlabs, PF10-03-P01). The distances from the sample to F_1 and F_2 are kept the same in the transmission and reflection arms, respectively. Finally, the reflection spectrum of the reference mirror $R_{\text{mirror}}(\lambda)$ was

measured separately (without the beam splitter). The estimated spectral one-sided absorption is $\mathcal{A}_1(\lambda) = 1 - \frac{T_{\text{sample}}(\lambda)}{T_{\text{ref}}(\lambda)} - \frac{R_{\text{sample}}(\lambda)}{R_{\text{ref}}(\lambda)} R_{\text{mirror}}(\lambda)$.

Impact of substrate change on mirror reflectivity

While the design methodology for obtaining $\mathcal{A}_1$ and $\mathcal{A}_2$ presupposes that incidence on mirror M_1 takes place from the cavity defect layer (Si here), in measurements, typically incidence is from air. To convert the mirror reflectivity R^{Si} in the former to that of the latter R^{air}, it is more convenient to use transfer matrices than scattering matrices. If the transfer matrix for incidence from Si is $\mathbf{T}^{\text{Si}}$ and from air is $\mathbf{T}^{\text{air}}$, it may be shown that they are connected through

$$\mathbf{T}^{\text{air}} = \frac{1}{2}\begin{pmatrix} 1+n & 1-n \\ 1-n & 1+n \end{pmatrix} \mathbf{T}^{\text{Si}},$$

where n is the refractive index of Si, and the elements of the transfer matrix $\mathbf{T}$ are related to those of the scattering matrix $\mathbf{S}$, through $\mathbf{T} = \frac{1}{t_{\text{L}}}\begin{pmatrix} 1 & -r_{\text{R}} \\ r_{\text{L}} & t_{\text{L}}t_{\text{R}} - r_{\text{L}}r_{\text{R}} \end{pmatrix}$. As such, the reflection and transmission coefficients after changing the incident material are related through

$$r_{\text{L}}^{\text{air}} = \frac{r^{\text{air,Si}} + r_{\text{L}}^{\text{Si}}}{1 + r^{\text{air,Si}} r_{\text{L}}^{\text{Si}}} \quad , \quad t_{\text{L}}^{\text{air}} = \frac{t^{\text{air,Si}} t_{\text{L}}^{\text{Si}}}{1 + r^{\text{air,Si}} r_{\text{L}}^{\text{Si}}}$$

where $r^{\text{air,Si}} = \frac{1-n}{1+n}$ and $t^{\text{air,Si}} = \frac{2}{1+n}$.

Using these relationships, one may predict the mirror reflectivity as measured for incidence from air shown in Fig 5-5c from the theoretical model of mirror reflectivity for incidence from Si shown in Fig. 5-5b.

5.1. Symmetric FP resonator

Optical device characterization.

We now proceed to the optical characterization of the complete symmetric device (Fig. 5-6a,b) in the one-sided-incidence configuration, carried out using the optical setup shown schematically in Fig. 5-6c for normally incident light. Making use of a collimated incoherent beam from a Tungsten lamp, we measure the transmission coefficient T_{L}, normalized with respect to the incident beam, and the reflection coefficient R_{L}, normalized with respect to a silver mirror, from which we determine the one-sided absorption $\mathcal{A}_1 = 1 - R_{\mathrm{L}} - T_{\mathrm{L}}$. These measurements are in contradistinction to all reported CPA measurements, which have been performed with coherent light.

We plot the measured values of R_{L}, T_{L}, and $\mathcal{A}_1$ as a function of wavelength in Fig. 5-6g-i compared to the corresponding calculated quantities given in Fig. 5-6d-f obtained using the transfer-matrix method. The spectral phase of reflection from M_1, $\alpha(\lambda)$, and the refractive index of Si, $n_{\mathrm{Si}}(\lambda)$, determine the *locations* of the resonances through $\alpha(\lambda) + \frac{2\pi}{\lambda} n_{\mathrm{Si}}(\lambda) d = m\pi$ (the resonance order m is an integer [31]). The *strength* of the resonances is set by the fidelity of the achieved R (for M_1) to the target design (Fig. 5-2c). In our calculations, we made use of the measured $n_{\mathrm{Si}}(\lambda)$ (see Fig. 5-3 for ellipsometric measurements over the spectral range of interest). In comparing the measurements and theoretical predictions of R_{L}, T_{L}, and $\mathcal{A}_1$ for the symmetric device, we note that the greatest deviation is in the vicinity of $\lambda = 1300$ nm, where the reflectivity of M_1 departs from the target values (Fig. 5-5c). A similar deviation occurs at the

short wavelength edge (~ 800 nm). In general, reaching the theoretical value of $\mathcal{A}_1 = 0.5$ at any resonance is readily predicted by the proximity of R to the target.

We have carried out one-sided-incidence measurements on the asymmetric device and compared the measured and theoretically predicted values of R_{L}, T_{L}, and $\mathcal{A}_1^{(\mathrm{a})}$ over a full spectral octave in Fig. 5-8. In contrast to $\mathcal{A}_1$ in Fig. 5-6, $\mathcal{A}_1^{(\mathrm{a})}$ is substantially larger than the symmetric-device-limit of $\mathcal{A}_1 \geq \frac{1}{2}$. We also superimpose the measured single-pass absorption $\mathcal{A}$ of Si (Fig. 5-2b) on the measured and predicted $\mathcal{A}_1^{(\mathrm{a})}$. We note again that deviations from achieving the theoretical limit of $\mathcal{A}_1^{(\mathrm{a})} = 1$ are associated with inaccuracies in mirror fabrication, which manifest themselves in differences between the target and measured reflectivities. Our measurements in Fig. 5-5 / Fig. 5-7 and statistical calculations in Chapter 5.3. indicate that there is ~ 5% error in the layer thicknesses of the fabricated mirrors. Reducing this error to ~ 2%, which may be readily achieved by the optical thin-film industry, makes the resulting deviations in mirror reflectivity have negligible impact on the effective absorption.

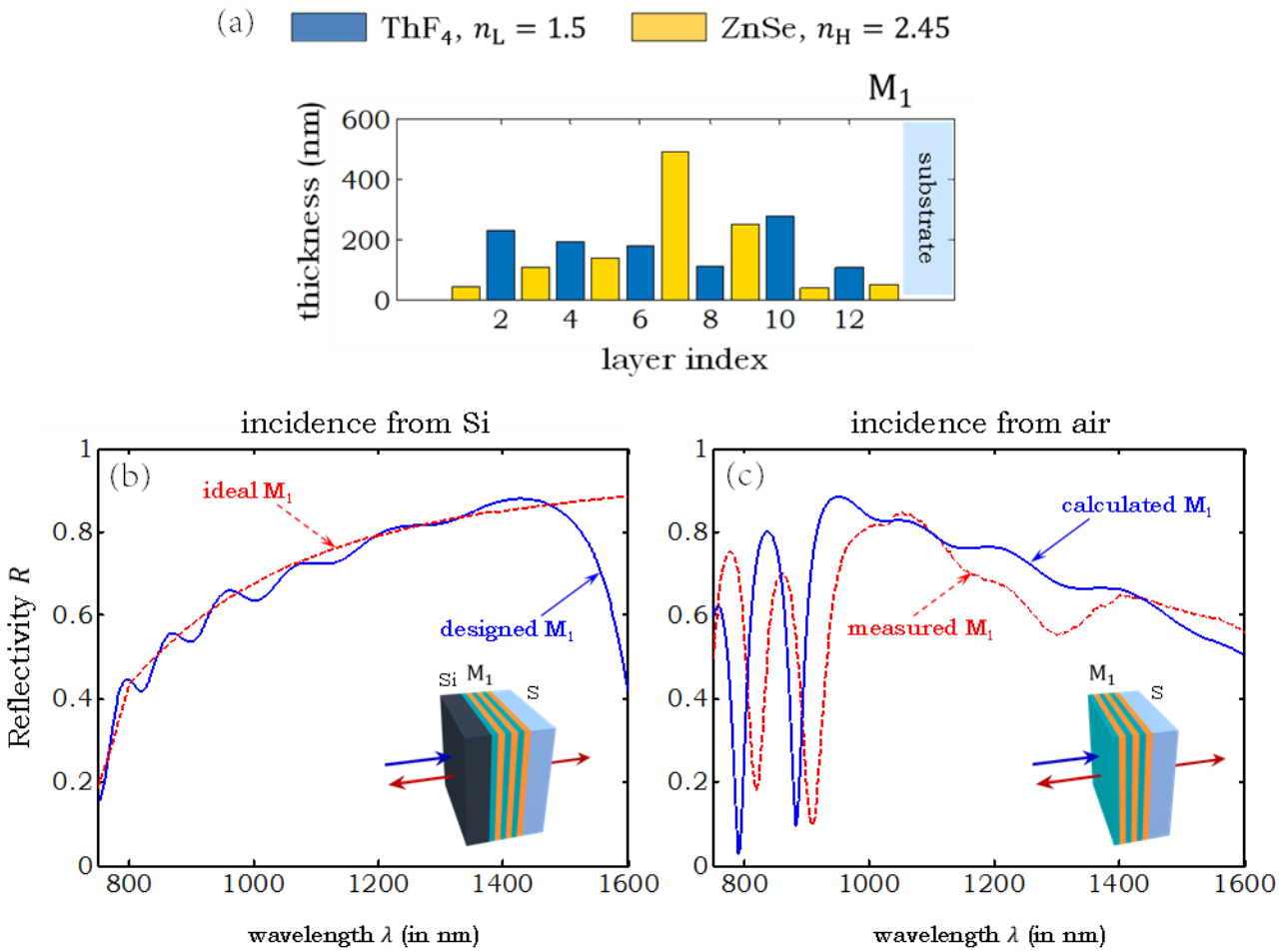

Figure 5-5: Symmetric mirror design for optimized CPA. (a) Thicknesses of the layers in the designed mirror M_1. The layers start from air on the left (Si in the case of the full device) to the substrate on the right. (b) The calculated spectral reflectivity $R(\lambda)$ of the mirror M_1 from (a) on a glass substrate S, solid curve, compared to the target reflectivity, dashed curve, from Fig. 5-2c. Incidence is from the Si (see inset). (c) Calculated (solid curve) and measured (dashed curve) reflectivity of the fabricated mirror M_1 on a glass substrate S for incidence from air (see inset).

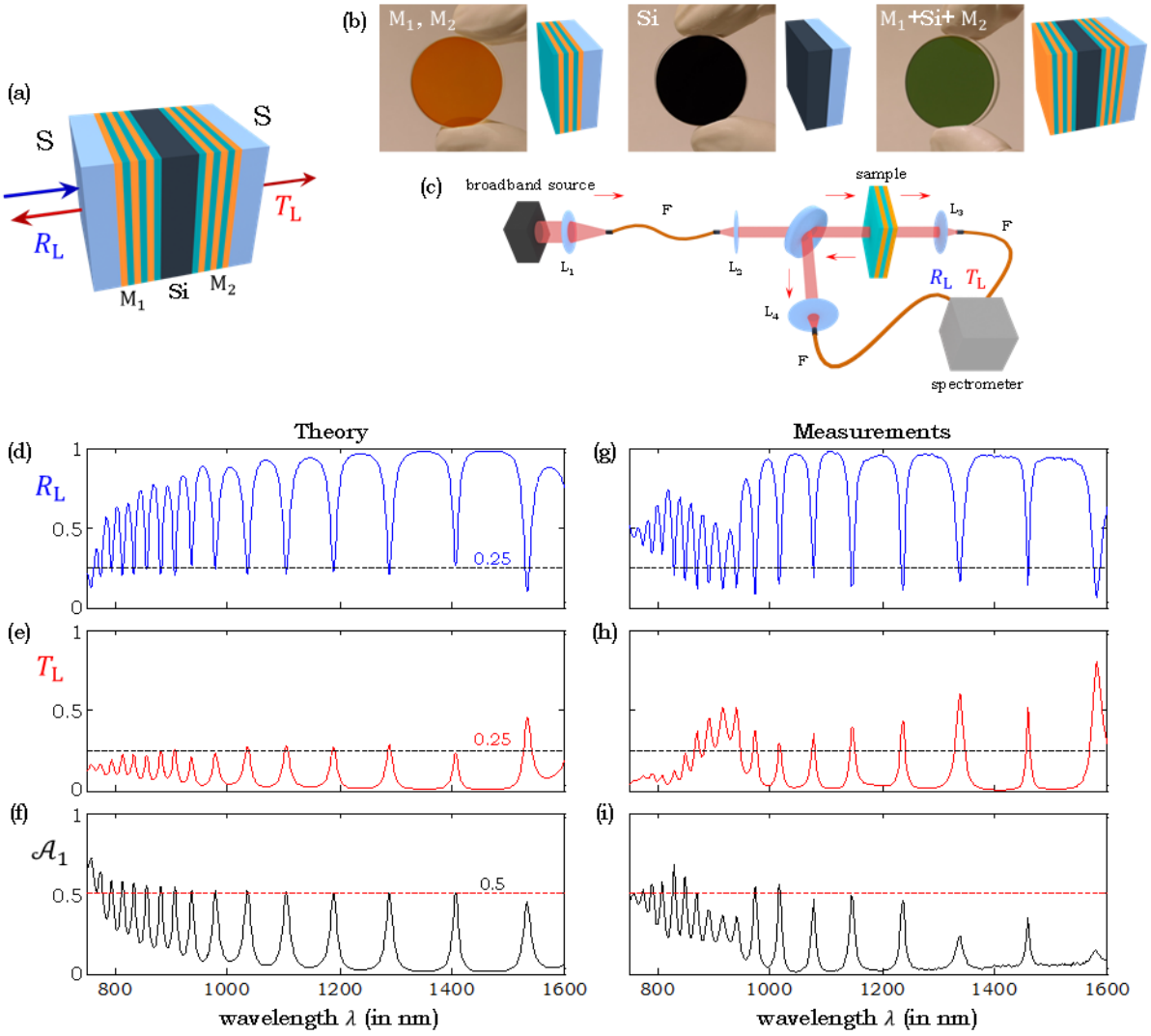

Figure 5-6: Measurements and theory for coherent one-sided absorption in the ZnSe/ThF₄ multilayer mirror symmetric FP resonator. (a) Schematic of the full device structure: S+M₁+Si+M₂+S. (b) Photographs of 25-mm-diameter samples: mirror M₁ (2.2-μm-thick), thin Si film (2-μm-thick), and the device M₁+Si+M₂ (6.4-μm-thick), all on BK7 substrates. (c) Schematic of the optical measurement setup. (d)-(f) Theoretical predictions of the spectral dependence of R_L, T_L, and $\mathcal{A}_1$ for the full S+M₁+Si+M₂+S structure obtained using transfer-matrix calculations, and (h)-(j) the corresponding measured spectral dependence. The dotted horizontal lines correspond to the ideal theoretical limits for optical coherent absorption in a symmetric structure for a one-sided-incidence configuration.

5.2. Asymmetric FP resonator

In an asymmetric structure with mirrors $\mathrm{M}_1^{(\mathrm{a})}$ and $\mathrm{M}_2^{(\mathrm{a})}$, if the reflectivity of $\mathrm{M}_2^{(\mathrm{a})}$ is unity, it was shown in Chapter 3.2 that choosing the reflectivity of $\mathrm{M}_1^{(\mathrm{a})}$ to be $R_1^{(\mathrm{a})} = (1-\mathcal{A})^2$ indeed eliminates reflection altogether and results in perfect one-sided absorption $\mathcal{A}_1^{(\mathrm{a})} = 1$. Comparing $R_1^{(\mathrm{a})}$ in Fig. 5-7b with R_2 in Fig. 5-2c shows that $R_1^{(\mathrm{a})} \leq R_2$, which is typically easier to achieve from the perspective of fabrication. A critical advantage of this configuration is that complete absorption is realized at *all* the resonances, such that twice the total absorption is produced here for one-sided incidence compared to that realized in a symmetric structure in the CPA condition for two-sided incidence.

We have carried out one-sided-incidence measurements on the asymmetric device and compared the measured and theoretically predicted values of R_{L}, T_{L}, and $\mathcal{A}_1^{(\mathrm{a})}$ over a full octave in Fig. 5-7. In contrast to $\mathcal{A}_1$ in Fig. 5-5, $\mathcal{A}_1^{(\mathrm{a})}$ is substantially larger than the symmetric-device-limit of $\mathcal{A}_1 \geq \frac{1}{2}$. We also superimpose the measured single-pass absorption $\mathcal{A}$ of Si (Fig. 5-2b) on the measured and predicted $\mathcal{A}_1^{(\mathrm{a})}$.

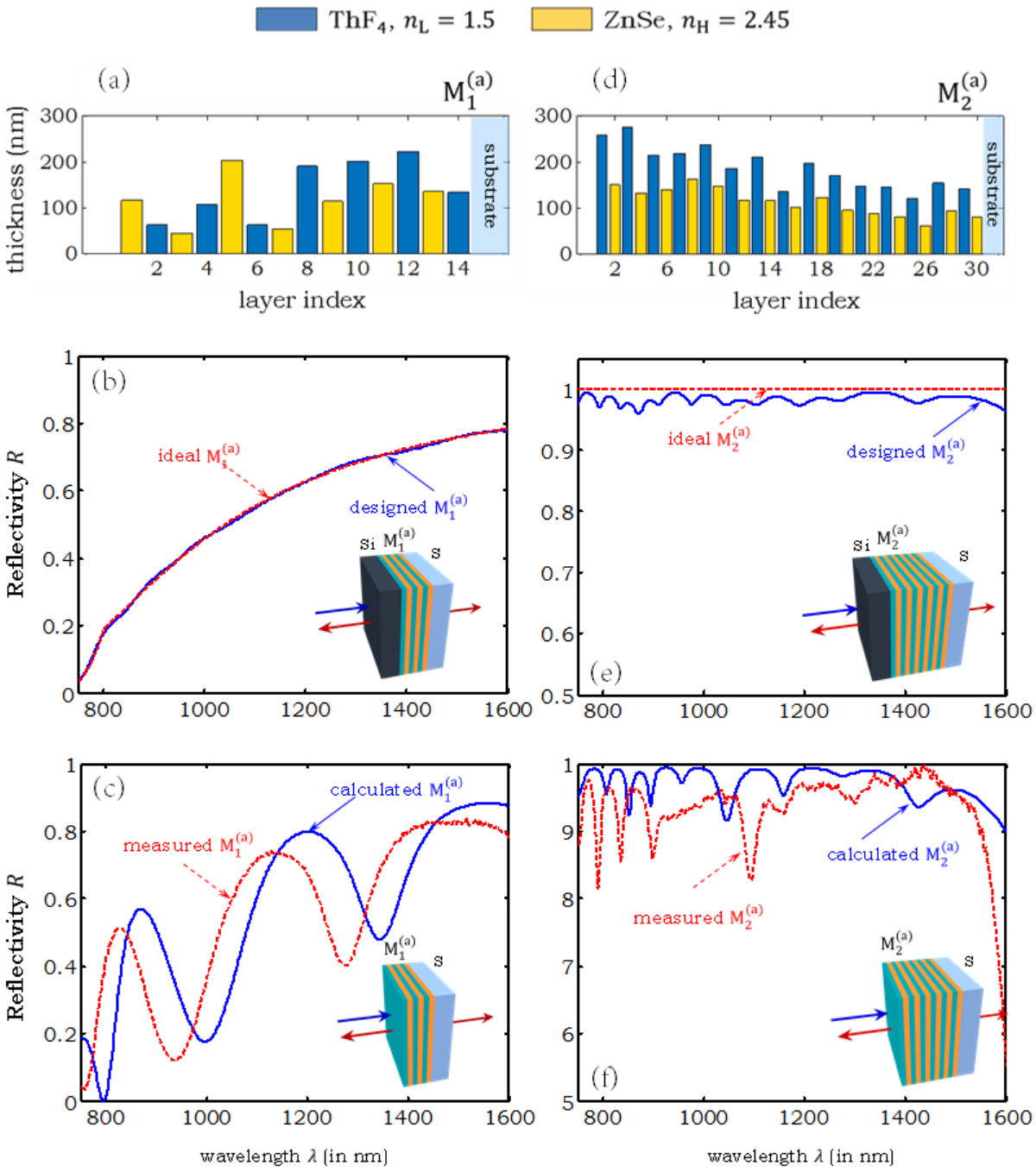

Figure 5-7: Asymmetric mirror design for optimized CPA. (a) Thicknesses of the layers in the designed mirror $M_1^{(a)}$. The layers start from air on the left (Si in the case of the full device) to the substrate on the right. (b) The calculated spectral reflectivity $R(\lambda)$ of the design mirror $M_1^{(a)}$ from (a) on a glass substrate S, solid curve, compared to the target reflectivity, dashed curve, from Fig. 5-2c. Incidence is from the Si (see inset). (c) Calculated (solid curve) and measured (dashed curve) reflectivity of the fabricated mirror $M_1^{(a)}$ on a glass substrate S for incidence from air (see inset). (d-f) same for ZnSe/ThF4 mirror $M_2^{(a)}$ with total reflectivity.

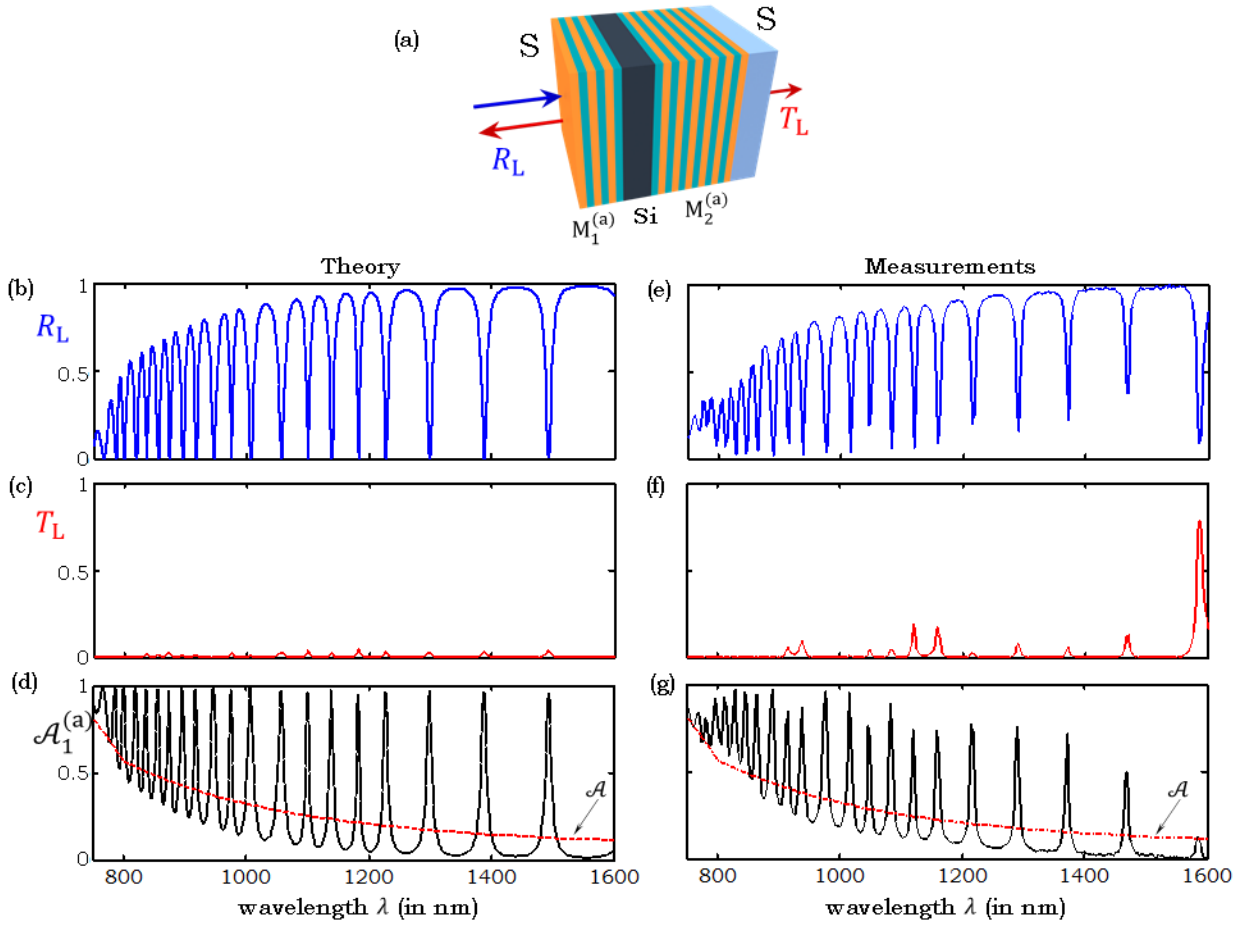

Figure 5-8: Measurements and theory for coherent perfect one-sided absorption in the ZnSe/ThF₄ multilayer mirror asymmetric FP resonator. (a) Schematic of the full device structure: $M_1^{(a)}$+Si+$M_2^{(a)}$+S. (b)-(d) Theoretical predictions of the spectral dependence of R_L, T_L, and $\mathcal{A}_1^{(a)}$ for the full $M_1^{(a)}$+Si+$M_2^{(a)}$+S structure obtained using transfer-matrix calculations, and (e)-(g) the corresponding measurements. The dotted lines in (d) and (g) correspond to the single-pass absorption $\mathcal{A}$ of a 2-μm-thick Si layer from Fig. 5-2b.

5.3. Theoretical study of the design robustness

Accuracy of the mirror design

We present here the results of our statistical investigation of the impact of fabrication errors on mirror reflectivity. We show an example in Fig. 5-9 where we show individual realizations at three different members of ensembles with average errors $\frac{\Delta d}{d}$ of 5% and 10% compared to the ideal case of 0% (the target design).

We examine two classes of fabrication errors: (1) percentile errors in layer thicknesses (Figs. 5-10, 5-11), and (2) absolute errors in layer thicknesses (Figs. 5-12, 5-13).

Effect of fabrication tolerances on multilayer film reflectivity

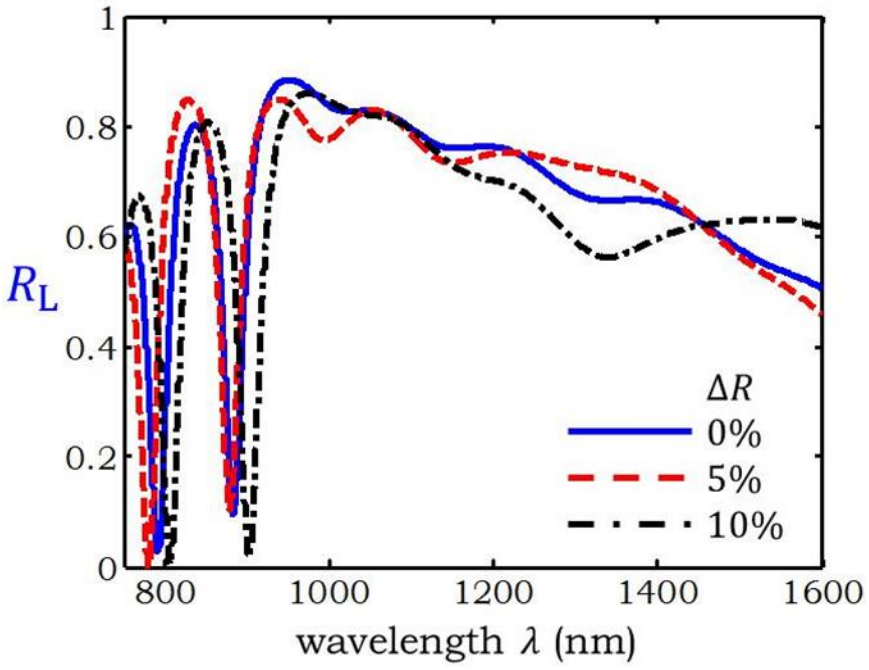

Figure 5-9: Effect of fabrication tolerances on multilayer film reflectivity. Two examples (from an ensemble of statistical realizations) of the spectral reflectivity $R(\lambda)$ of mirror M_1 when random fabrication errors are introduced into the layer thicknesses, corresponding to $\Delta R = 5\%$ and 10% random errors in each layer thickness. In each case, we assume that the errors have a uniform probability density function with width ΔR. The mirror with $\Delta R = 0\%$ corresponds to the target mirror reflectivity in Fig. 5-5c in chapter 5.1 (incidence from air).

Effect of fabrication tolerances of **relative** layer thicknesses on multilayer film reflectivity

Incidence from air:

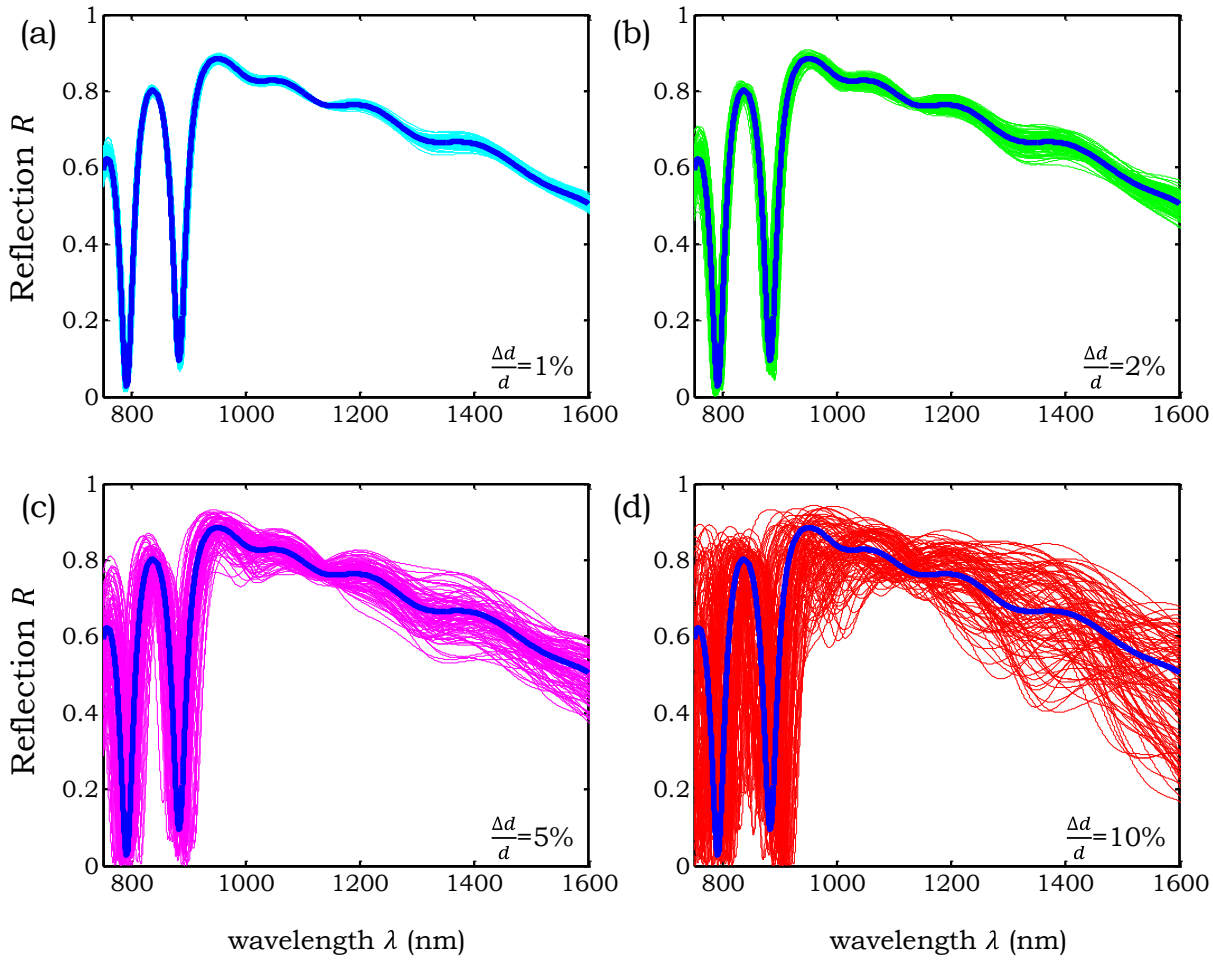

Figure 5-10: Solid thick line corresponds to the target 13-layer mirror M_1 reflectivity R for incidence from air. Overlaid are an ensemble of 100 realizations of R in the presence of relative errors in the layer thicknesses (a) $\frac{\Delta d}{d} = 1\%$, (b) 2%, (c) 5%, and (d) 10%. In each ensemble, the probability distribution for the thickness of each layer is taken to be uniform with a mean equal to the target thickness and full width equal to the above values of $\frac{\Delta d}{d}$.

Effect of fabrication tolerances of **relative** layer thicknesses on multilayer film reflectivity

Incidence from Si:

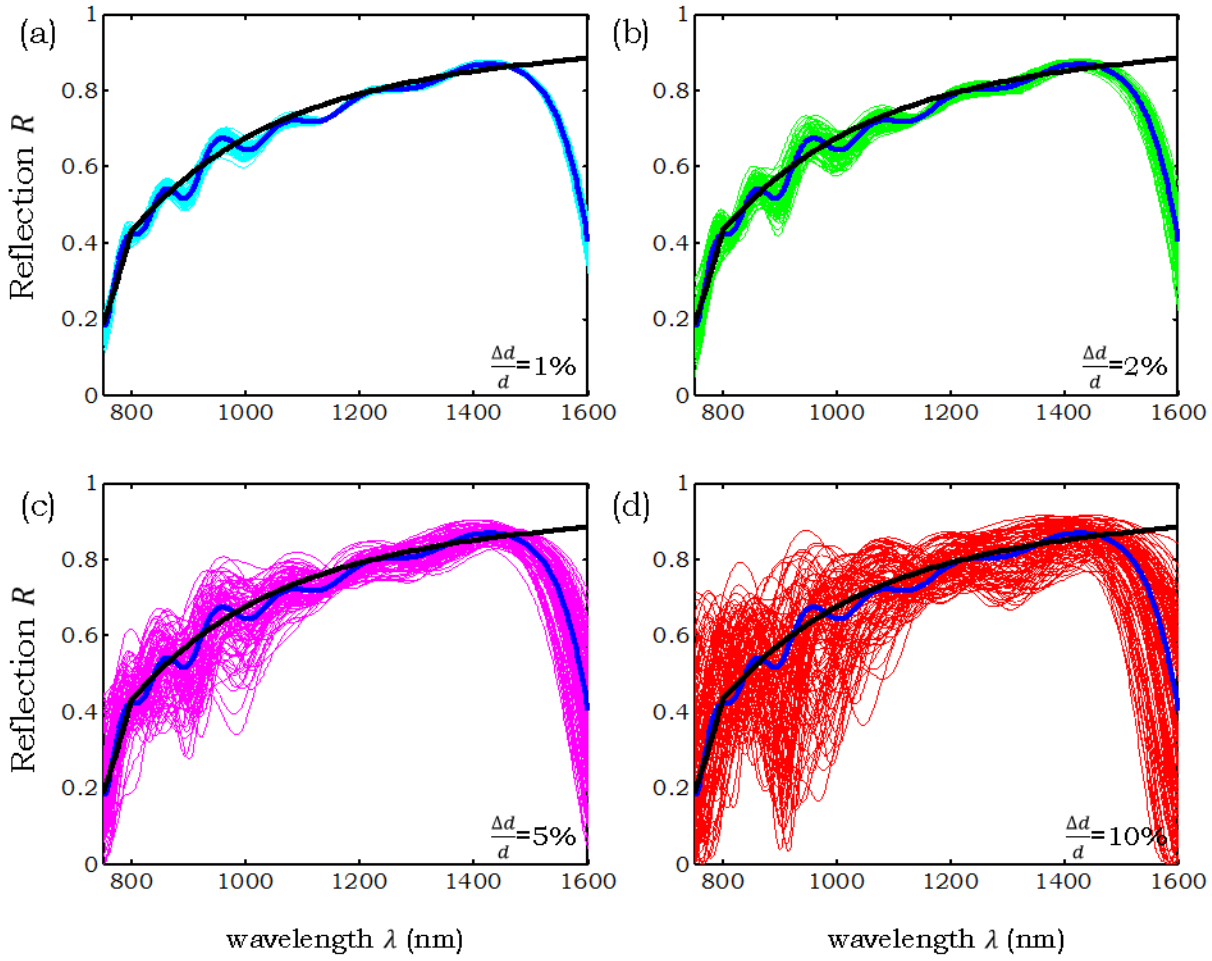

Figure 5-11: Solid thick line corresponds to the target 13-layer mirror M1 reflectivity R for incidence from Si. Overlaid are an ensemble of 100 realizations of R in the presence of relative errors in the layer thicknesses (a) Δd/d=1%, (b) 2%, (c) 5%, and (d) 10%. In each ensemble, the probability distribution for the thickness of each layer is taken to be uniform with a mean equal to the target thickness and full width equal to the above values of Δd/d.

Effect of fabrication tolerances of **absolute** layer thicknesses on multilayer film reflectivity

Incidence from air:

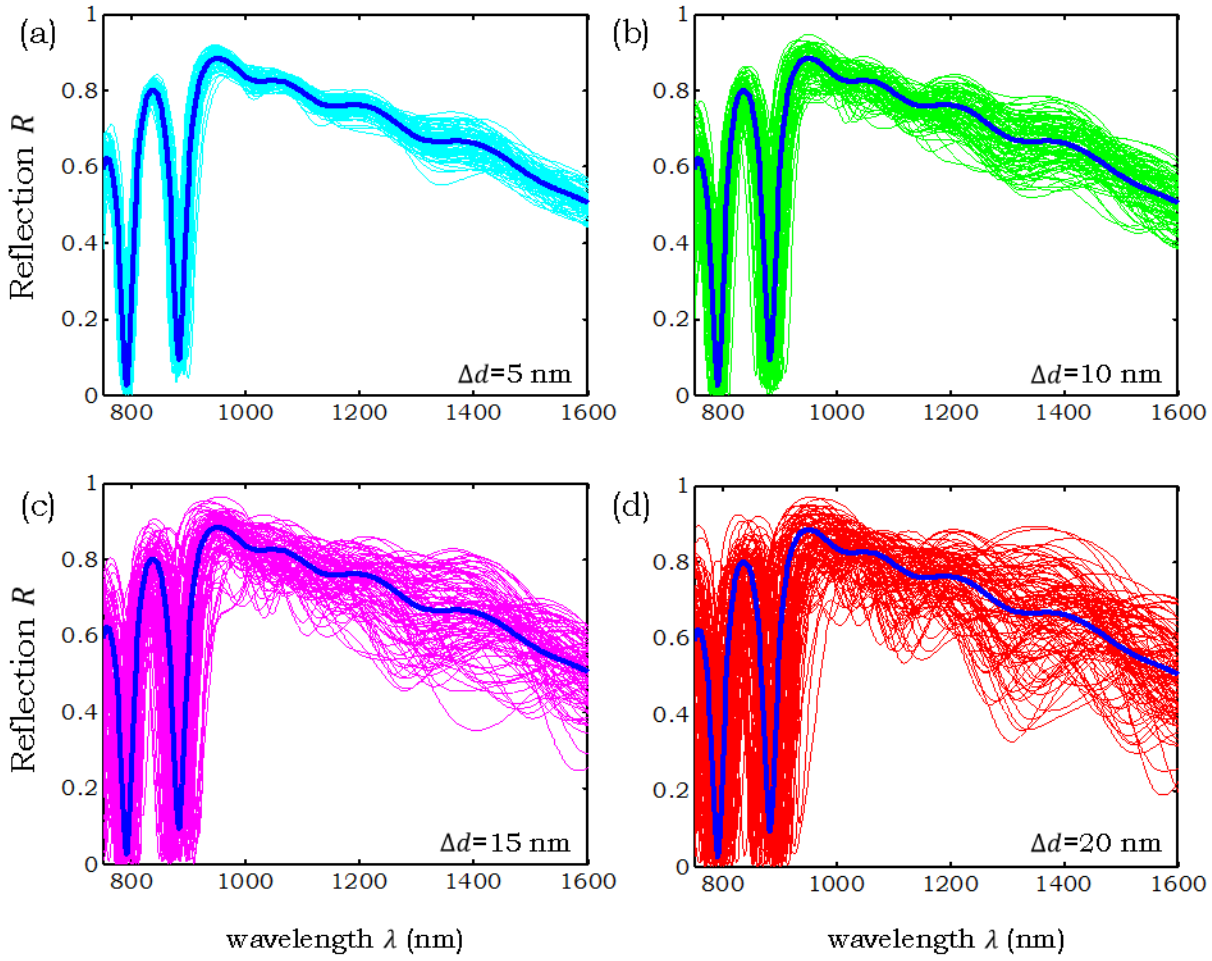

Figure 5-12: Solid thick line corresponds to the target 13-layer mirror M_1 reflectivity R for incidence from air. Overlaid are an ensemble of 100 realizations of R in the presence of absolute errors in the layer thicknesses (a) $\Delta d = 1\ nm$, (b) $5\ nm$, (c) $10\ nm$, and (d) $15\ nm$. In each ensemble, the probability distribution for the thickness of each layer is taken to be uniform with a mean equal to the target thickness and full width equal to the above values of Δd.

Effect of fabrication tolerances of **absolute** layer thicknesses on multilayer film reflectivity

Incidence from Si:

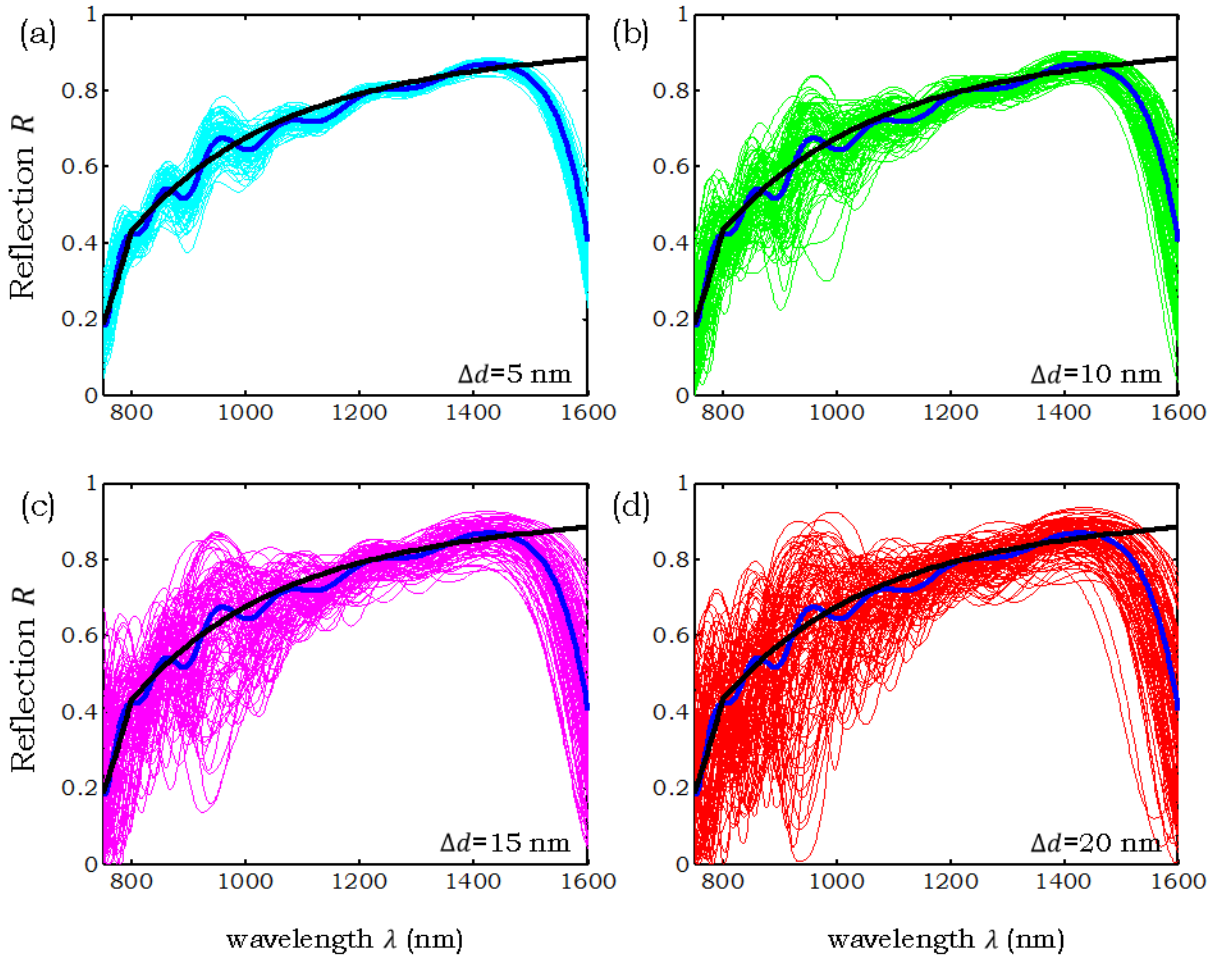

Figure 5-13: Solid thick line corresponds to the target 13-layer mirror M_1 reflectivity R for incidence from Si. Overlaid are an ensemble of 100 realizations of R in the presence of absolute errors in the layer thicknesses (a) $\Delta d = 1$ nm, (b) 5 nm, (c) 10 nm, and (d) 15 nm. In each ensemble, the probability distribution for the thickness of each layer is taken to be uniform with a mean equal to the target thickness and full width equal to the above values of Δd.

Impact of number of mirror layers on reflectivity

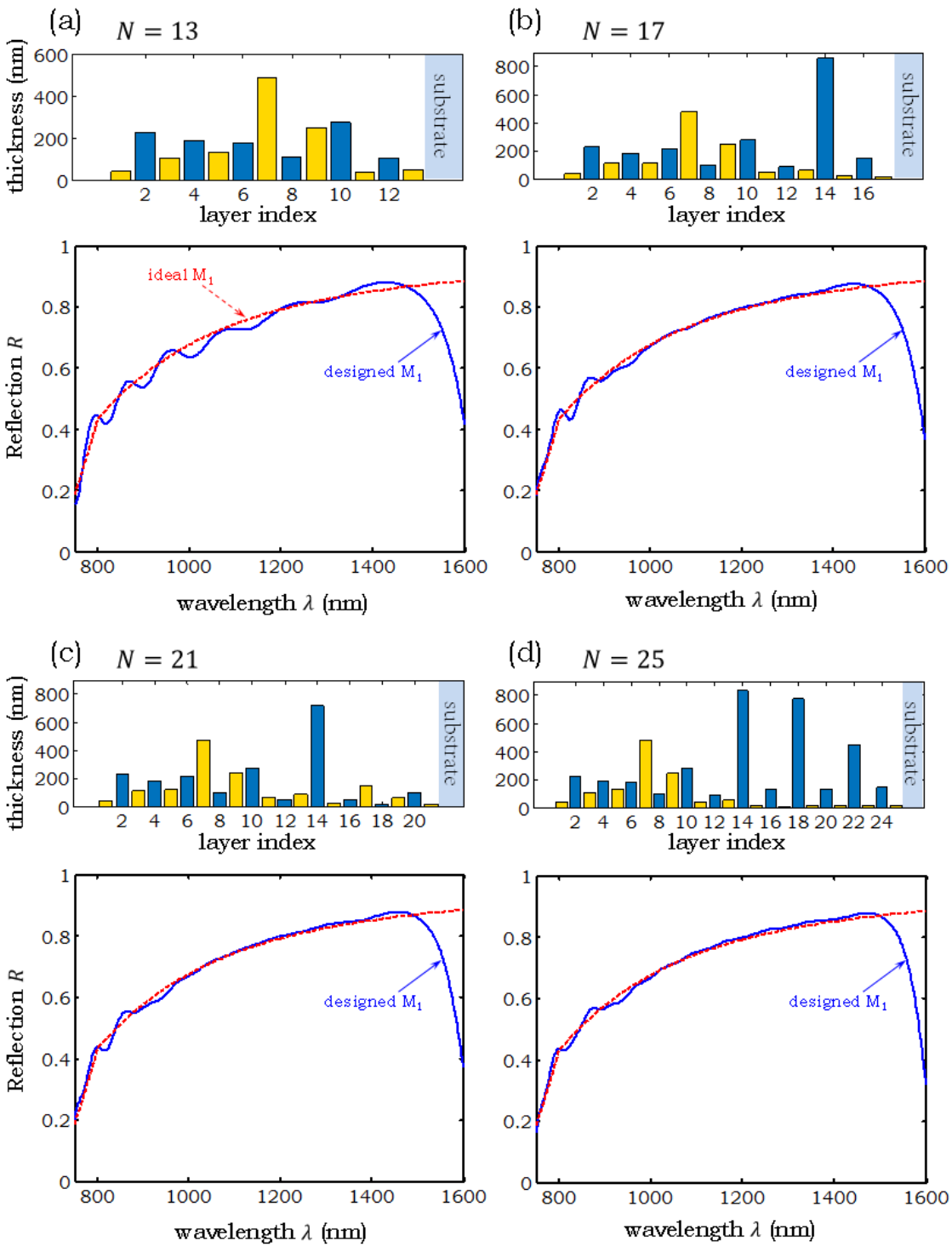

Figure 5-14: a)-(d) The structure and reflectivity R of the multilayer mirror M_1 with (a) $N = 13$, (b) $N = 17$, (c) $N = 21$, and (d) $N = 25$ layers. In each panel we plot the sequence of layer thicknesses (top half) and also compare the calculated R assuming incidence from Si with respect to the ideal R from Fig. 5-4b (bottom half).

5.4. Discussion

A milestone in the development of ultrabroad-bandwidth lasers [21] was the realization that chirped mirrors [22,23] with spectrally flat reflection amplitude enable control over the cavity dispersion via their spectral *phase*, which is necessary to produce ultrashort pulses. We have shown here that in lossy cavities, the bandwidth of the CPA effect is increased through control over the spectral *amplitude* of the mirror reflectivities and not the phase. By implementing this principle, we have demonstrated coherent perfect absorption over a full octave of bandwidth (~800 – 1600 nm) that is dramatically broader than previous experimental results. Plasmonics-[15,16] and metamaterials-based [17] realizations have been restricted to a single wavelength, while the Si-based experiment in Ref. [8] was carried out by tuning a continuous-wave laser over a 3-nm bandwidth in a 100-μm-thick Si film.

We have focused here on optical absorption in Si, but our approach is applicable to any other material that may be processed into a film. Resonant absorption in organic dyes, for example, may also be exploited through the use of mirrors with a 'dip' in reflectivity corresponding to the resonant 'peak' in absorption, as dictated by the design principle in Fig. 5-2a. Nevertheless, there are practical limits for the extent to which this approach may be applied. Specifically, layers with very small intrinsic absorption $\mathcal{A}$ will require very high R and are less tolerant to perturbations resulting from finite fabrication tolerances. Future efforts will be devoted to addressing the challenge of extending the CPA effect to continuously cover the spectrum (a promising approach is outlined in Chapter 6), essentially 'filling in' the gaps between the

resonances – potentially by exploiting the concept of white light cavities [24] or optimizing the mirror structure with respect to both the reflectivity amplitude *and* phase [33].

Our results demonstrate that the judicious design of the photonic environment in which a layer of a lossy material is embedded allows one to controllably sever the link between the effective optical absorption in a structure and the intrinsic absorption of the material from which it is constructed. The bandwidth over which such control may be exercised is only limited by the ultimate fabrication precision, and may extend for several octaves.

We have thus created the basis for a transformative method that helps address a host of critical photonic challenges, including cost-effective harnessing of infrared solar energy, achieving flat spectral sensitivity for photodetectors, and maximizing pump absorption in lasers using only planar technology. The device design strategy we have presented may be readily extended to on-chip implementations other than the planar structures reported here, which may relax the materials constraints for efficient on-chip optical detection [25], strong-coupling with resonant materials [26], and ultra-sensitive detection of pathogens [27].

6. MODEL FOR CONTINUOUS RESONANCE BROADBAND CPA

In our analysis in Chapter 3 we have theoretically shown that the spectral locations of the CPA resonances are affected by the phase α(λ) of the reflection from mirror M_1. One way to change the spectral phase α(λ) of the reflection from mirror M_1 is to vary the incidence angle of the incoherent light beam into the device. This effect was simulated computationally over a 90° input span, see Fig. 6-1.

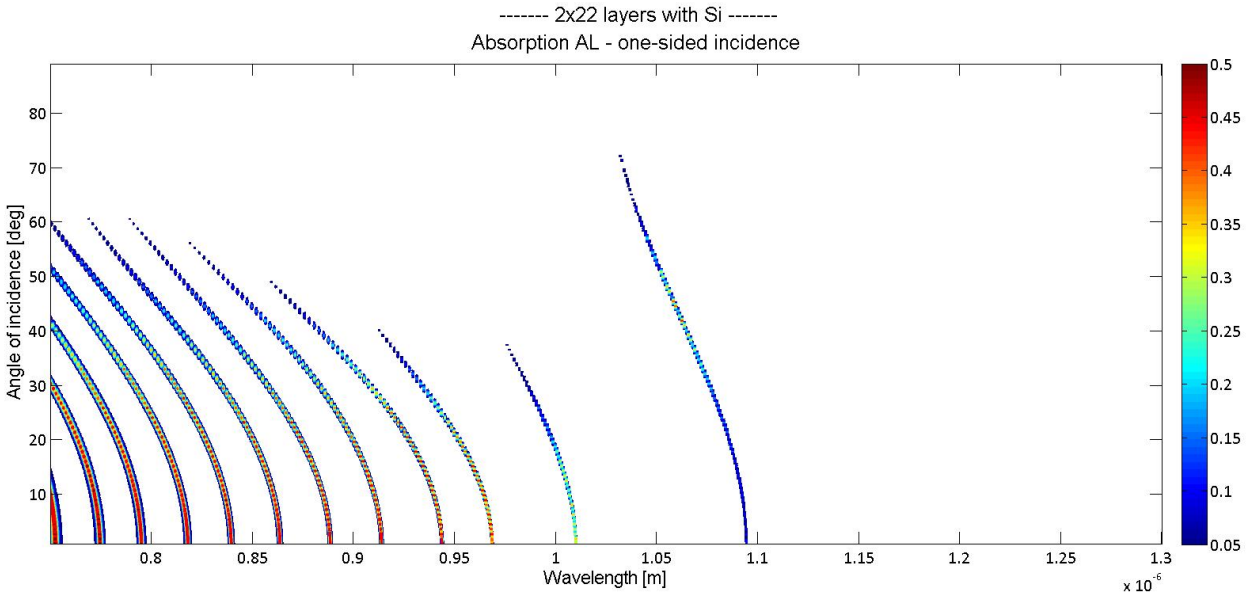

Figure 6-1: Absorption AL of the computational model in Chapter 3 over the near-infrared bandwidth as a function of the angle of incidence of a beam of incoherent light.

Interestingly, with increasing angle of incidence the resonances migrate to the shorter wavelength side of the spectrum, which is in opposition to the effect from conventional diffraction gratings, where shorter wavelengths are diffracted less than longer ones.

The functional shapes of the wavelength-dependent absorption functions shown in Fig. 6-1 are roughly cosine-shaped in the span of interest, see Fig. 6-2 below.

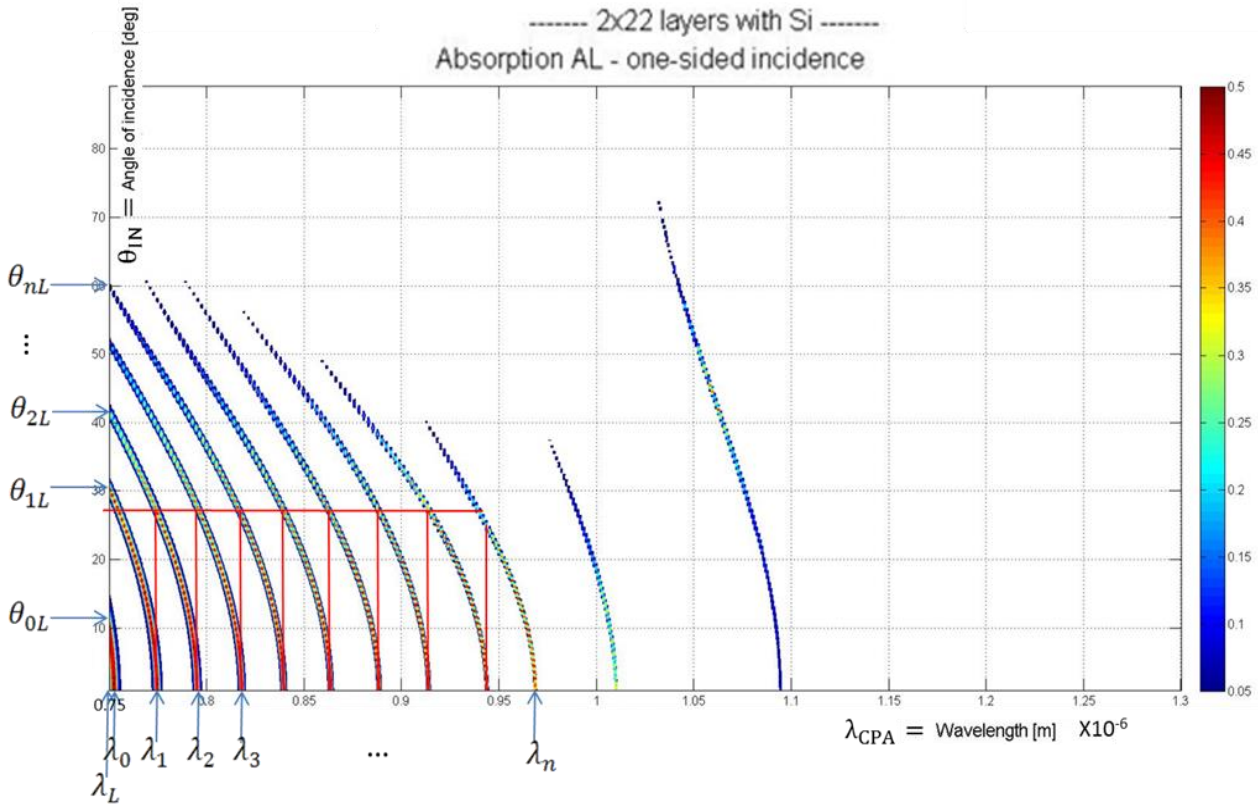

$$\lambda_{CPA} = (\lambda_n - \lambda_L)\cos\left(\frac{\pi}{2}\frac{\theta_{IN}}{\theta_{nL}}\right) + \lambda_L \qquad \theta_{IN} = \frac{\theta_{nL}}{\pi/2} arccos\left(\frac{\lambda_{CPA} - \lambda_L}{\lambda_n - \lambda_L}\right)$$

Figure 6-2: Cosine approximation of the incidence-dependent absorption functions.

We have seen in the previous chapter that the number and strength of CPA resonances is maximized in the asymmetric mirrors configuration of our experimental device. Improved selections of mirror and dielectric materials may also improve the bandwidth coverage.

We have also theoretically shown that the spectral locations of the CPA resonances are affected by the phase α(λ) of the reflection from mirror $M_1^{(a)}$. As Fig. 6-3 below shows, the asymmetric device exhibits the additional advantage over the symmetric device, that the individual resonant wavelengths expand into a series of thicker, almost continuous bands. The challenge

facing us is to engineer a diffraction capability that will achieve broadening, as well as compacting the CPA resonances.

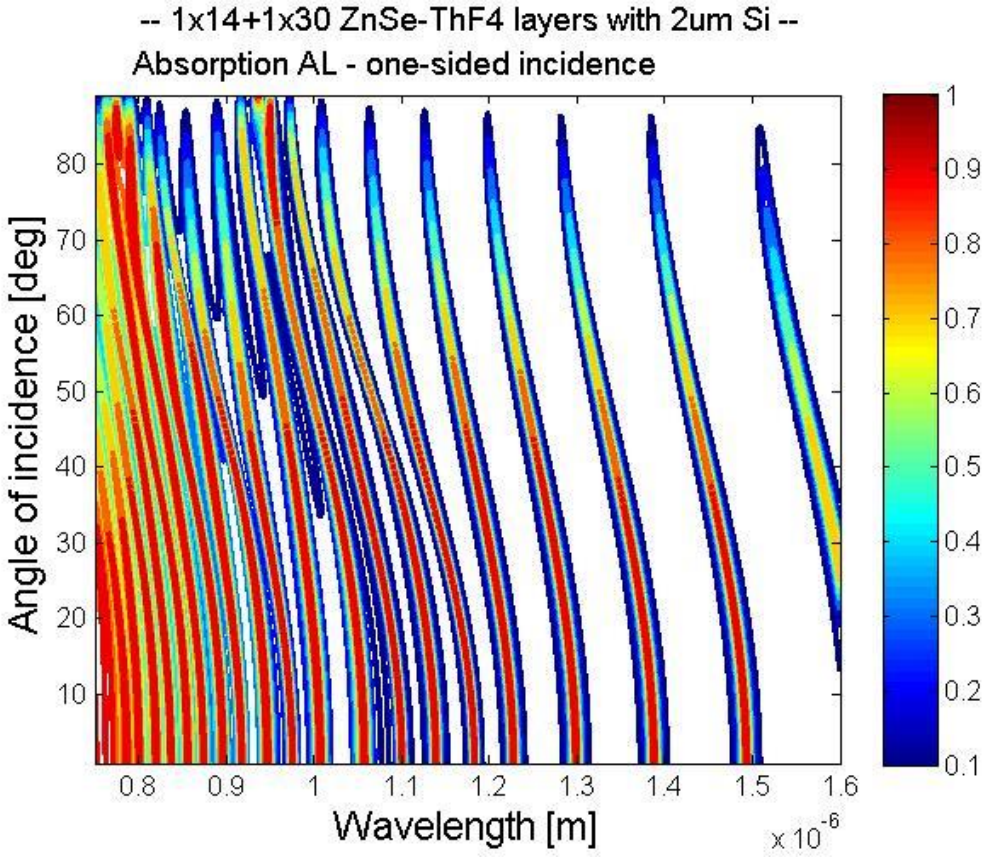

Figure 6-3: Varying the incidence angle on the asymmetric device.

A recently published study [32] by England et al. describes how a new type of quasi-planar grating, inspired by the reflective structure in the wings of the *Pierella luna* butterfly (see Fig. 6-4 and 6-5), may help us overcome the physical limitation of conventional gratings and allow us to fill in the gaps in the CPA resonances by designing a reverse-diffraction grating geometry to diffract the light incident into our device into a spectral distribution that compacts the bands shown in Fig. 6-3 into a continuously maximized resonance band across the full octave.

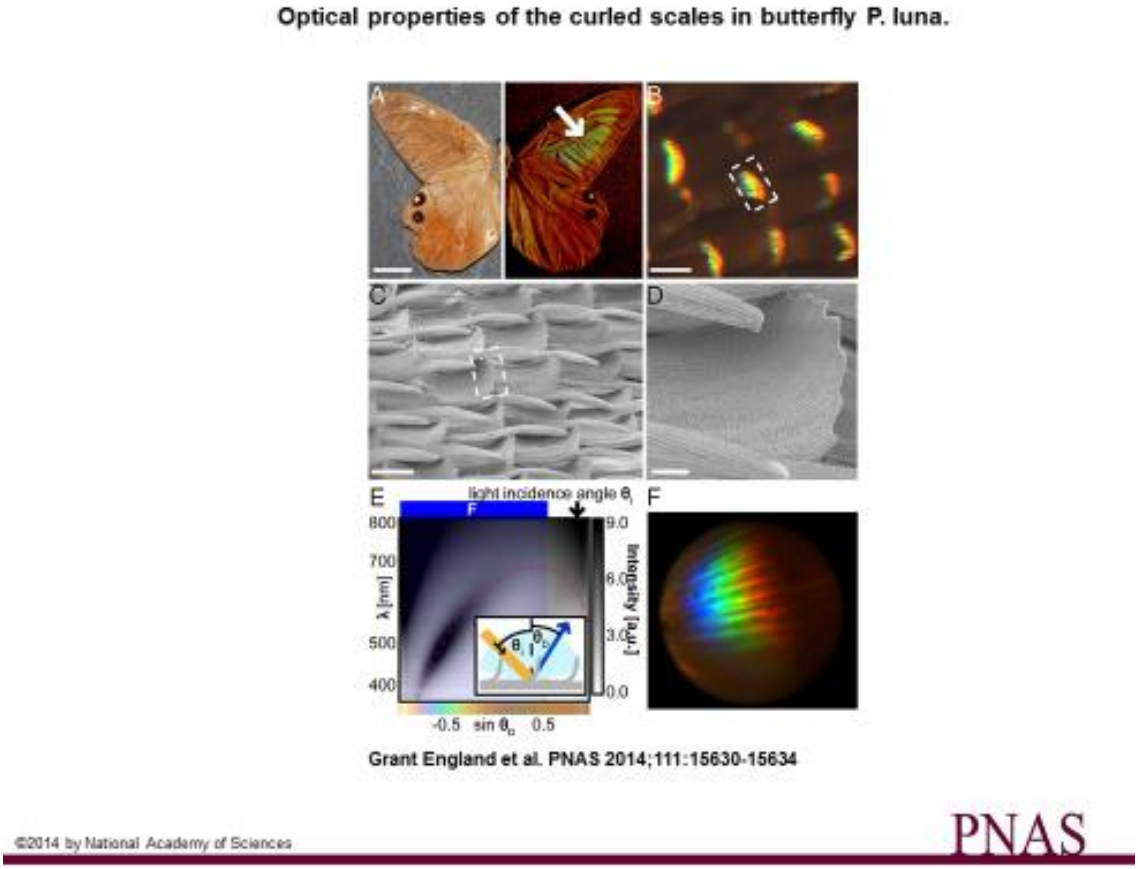

Figure 6-4: Optical properties of the curled scales in butterfly P. luna (see Grant England et al. PNAS 2014;111:15630-15634).

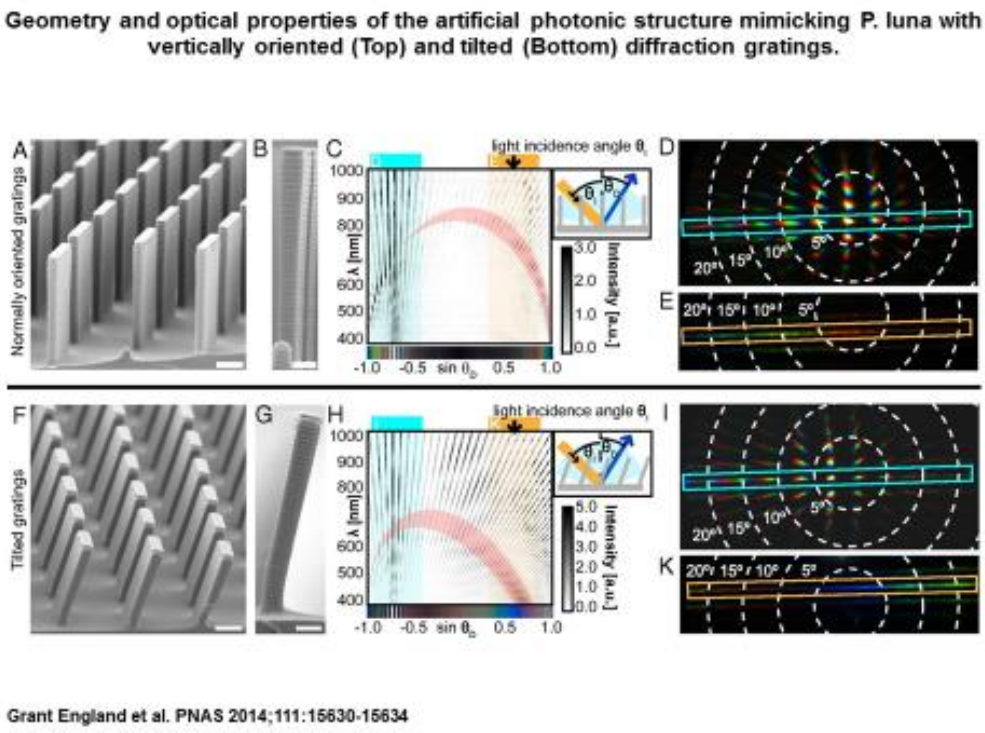

Figure 6-5: Geometry and optical properties of the artificial photonic structure mimicking P. luna with vertically oriented (Top) and tilted (Bottom) diffraction gratings (see Grant England et al. PNAS 2014;111:15630-15634).

The reverse diffraction achieved by the microdiffraction plates shown in Fig. 6-5 is described by the grating equation:

$$\lambda = \frac{d}{m}(\cos(\theta_I - \beta) + \cos(\theta_D - \beta))$$

Where d is the grating periodicity, m is the diffraction order, θ_I is the light incidence angle, θ_D is the diffraction angle, and β is the tilt angle of the microplates relative to the surface normal.

In a follow-on study we will strive to use this novel diffraction grating concept to achieve continuous broadband CPA.

LIST OF REFERENCES

[1] A. Guo, G. J. Salamo, D. Duchesne, R. Morandotti, M. Volatier-Ravat, V. Aimez, G. A. Siviloglou, and D. N. Christodoulides, ”Observation of PT-Symmetry Breakingin Complex Optical Potentials,” Phys. Rev. Lett. **103**, 093902 (2009).

[2] L. Feng, Y.-L. Xu, W. S. Fegadolli, M.-H. Lu, J. E. B. Oliveira, V. R. Almeida, Y.-F. Chen, and A. Scherer, ”Experimental demonstration of a unidirectional reflectionless parity-time metamaterial at optical frequencies,” Nat. Mater. **12**, 108 (2013).

[3] M. A. Kats, R. Blanchard, P. Genevet, and F. Capasso, ”Nanometre optical coatings based on strong interference effects in highly absorbing media,” Nat. Mater. **12**, 20 (2013).

[4] C. E. Rüter, K. G. Makris, R. El-Ganainy, D. N. Christodoulides, M. Segev, and D. Kip, ”Observation of parity-time symmetry in optics,” Nat. Phys. **6**, 192 (2010).

[5] A. Regensburger, C. Bersch, M.-A. Miri, G. Onishchukov, D. N. Christodoulides, and U. Peschel, ”Paritytime synthetic photonic lattices,” Nature **488**, 167 (2012).

[6] N. Bender, S. Factor, J. D. Bodyfelt, H. Ramezani, D. N. Christodoulides, F. M. Ellis, and T. Kottos, ”Observation of asymmetric transport in structures with active nonlinearities,” Phys. Rev. Lett. **110**, 234101 (2013).

[7] Y. D. Chong, L. Ge, H. Cao, and A. D. Stone, ”Coherent perfect absorbers: Time-reversed lasers,” Phys. Rev. Lett. **105**, 053901 (2010).

[8] W. Wan, Y. Chong, L. Ge, H. Noh, A. D. Stone, and H. Cao, ”Time-reversed lasing and interferometric control of absorption,” Science **331**, 889 (2011).

[9] Y. D. Chong and A. D. Stone, ”Hidden black: Coherent enhancement of absorption in strongly scattering media,” Phys. Rev. Lett. **107**, 163901 (2011).

[10] A. Yariv and P. Yeh, *Optical Waves in Crystals: Propagation and Control of Laser Radiation* (Wiley- Interscience, Hoboken, New Jersey, 2003).

[11] P. Yeh, *Optical Waves in Layered Media* (Wiley- Interscience, Hoboken, New Jersey, 2005).

[12] P. Markoˇs and C. M. Soukoulis, *Wave Propagation: From Electrons to Photonic Crystals and Left-Handed Materials* (Princeton Univ. Press, Princeton, New Jersey, 2008).

[13] M. A. Green, ”Self-consistent optical parameters of intrinsic silicon at 300 K including temperature coefficients,” Sol. Energ. Mat. Sol. C. **92**, 1305 (2008).

[14] S. Fathpour and B. Jalali, *Silicon Photonics for Telecommunications and Biomedicine* (CRC Press, 2012

[15] Z. Li, S. Zhang, N. J. Halas, P. Nordlander, and H. Xu, "Coherent modulation of propagating plasmons in silver-nanowire-based structures," Small **7**, 593–596 (2011).

[16] J. W. Yoon, G. M. Koh, S. H. Song, and R. Magnusson, "Measurement and modeling of a complete optical absorption and scattering by coherent surface plasmon-polariton excitation using a silver thin-film grating," Phys. Rev. Lett. **109**, 257402 (2012).

[17] J. Zhang, K. F. MacDonald, and N. I. Zheludev, "Controlling light-with-light without nonlinearity," Light: Science & Applications **1**, e18 (2012). doi:10.1038/lsa.2012.18

[18] S. Dutta-Gupta, O. J. F. Martin, S. Dutta Gupta, and G. S. Agarwal, "Controllable coherent perfect absorption in a composite film," Opt. Express **20**, 2246-2254 (2012).

[19] M. Pu, Q. Feng, M. Wang, C. Hu, C. Huang, X. Ma, Z. Zhao, C. Wang, and X. Luo, "Ultrathin broadband nearly perfect absorber with symmetrical coherent illumination," Opt. Express **20**, 2246-2254 (2012).

[20] J. Meiron, "Damped Least-Squares Method for Automatic Lens Design," Journal of the Optical Society of America **55**, 1105-1107 (1965).

[21] T. Brabec and F. Krausz, "Intense few-cycle laser fields: Frontiers of nonlinear optics," Rev. Mod. Phys. **72**, 545-591 (2000).

[22] R. Szipöcs, K. Ferencz, C. Spielmann, and F. Krausz, "Chirped multilayer coatings for broadband dispersion control in femtosecond lasers," Opt. Lett. **19**, 201-203 (1994).

[23] F. X. Kärtner, N. Matuschek, T. Schibli, U. Keller, H. A. Haus, C. Heine, R. Morf, V. Scheuer, M. Tilsch, and T. Tschudi, "Design and fabrication of double-chirped mirrors," Opt. Lett. **22**, 831-833 (1997).

[24] O. Kotlicki and J. Scheuer, "Wideband coherent perfect absorber based on white-light cavity," Opt. Lett. **39**, 6624-6627 (2014).

[25] N. M. M. Pires, T. Dong, U. Hanke, and N. Hoivik, "Recent developments in optical detection technologies in lab-on-a-chip devices for biosensing applications," Sensors **14**, 15458-15479 (2014).

[26] X. Liu, T. Galfsky, Z. Sun, F. Xia, E. Lin, Y.-H. Lee, S. Kéna-Cohen, and V. M. Menon, "Strong light-matter coupling in two-dimensional atomic crystals," Nat. Photon. **9**, 30-34 (2015).

[27] A. M. Armani, R. P. Kulkarni, S. E. Fraser, R. C. Flagan, and K. J. Vahala, "Label-free, single-molecule detection with optical microcavities," Science **317**, 783-787 (2007)

[28] J. A. Dobrowolski, “Completely automatic synthesis of optical thin film systems,” Appl. Opt. **4**, 937-946 (1965).

[29] D. A. B. Miller, “Fundamental limit for optical components,” J. Opt. Soc. Am. B **24**, A1-A18 (2007).

[30] A. Gumennik, E. C. Levy, B. Grena, L. Wei, C. Hou, T. Sarathi, A. F. Abouraddy, J. D. Joannopoulos, and Y. Fink, “Raindrop inspired effects in fibre microspheres,” unpublished.

[31] B. E. A. Saleh and M. C. Teich, *Fundamentals of Photonics* (Wiley, 2007), 2nd Ed.

[32] G. England, M. Kolle, P. Kim, M. Khan, P. Muñoz, E. Mazur, and J. Aizenberg, “Bioinspired micrograting arrays mimicking the reverse color diffraction elements evolved by the butterfly Pierella luna,” PNAS **44**, 15630–15634 (2014).

[33] J. Bechhoefer, “Kramers-Kronig, Bode, and the meaning of zero,” Am. J. Phys. **79**, 1053-1059 (2011).

[34] M. L. Villinger, M. Bayat, L. N. Pye, and A. F. Abouraddy, “Analytical model for coherent perfect absorption in one-dimensional photonic structures,” to be submitted for publication in Optics Letters.

[35] L. N. Pye, M. L. Villinger, S. Shabahang, W. D. Larson, L. Martin, and A. F. Abouraddy, “Octave-spanning optical coherent perfect absorption,” submitted for publication in Nature Photonics.